

# Spin-orbital magnetism in moiré Wigner molecules

Ahmed Khalifa,<sup>1</sup> Rokas Veitas,<sup>1</sup> Francisco Machado,<sup>2,3</sup> and Shubhayu Chatterjee<sup>1</sup>

<sup>1</sup>*Department of Physics, Carnegie Mellon University, Pittsburgh, PA 15213, USA*

<sup>2</sup>*ITAMP, Harvard-Smithsonian Center for Astrophysics, Cambridge, MA 02138, USA*

<sup>3</sup>*Department of Physics, Harvard University, Cambridge, MA 02138, USA*

The interplay of spin and orbital degrees of freedom offers a versatile playground for the realization of a variety of correlated phases of matter. However, the types of spin-orbital interactions are often limited and challenging to tune. Here, we propose and analyze a new platform for spin-orbital interactions based upon a lattice of Wigner molecules in moiré transition metal dichalcogenides (TMDs). Leveraging the spin-orbital degeneracy of the low-energy Hilbert space of each Wigner molecule, we demonstrate that TMD materials can host a general spin-orbital Hamiltonian that is tunable via the moiré superlattice spacing and dielectric environments. We study the phase diagram for this model, revealing a rich landscape of phases driven by spin-orbital interactions, ranging from ferri-electric valence bond solids to a helical spin liquid. Our work establishes moiré Wigner molecules in TMD materials as a prominent platform for correlated spin-orbital phenomena.

The complex interplay between orbital and spin degrees of freedom lies at the heart of some of the most exciting correlated many-body electronic phenomena [1–13]. In the context of quantum magnetism, spin-orbit coupling (SOC) is often responsible for the kinds of anisotropy and exchange frustrations that stabilize quantum spin liquid states [1–3], while in spintronics, the coupling between electric and magnetic orders in multiferroics enables the electrical control of magnetism [14–20]. Observing this wealth of phenomena depends on our ability to control and engineer the underlying spin-orbit interactions. Moiré materials, due to their tunability, offer a new landscape to explore correlated physics [21–23]. However, the most commonly considered spin-orbital interactions are limited to spin-valley locking via Ising SOC [24–27], or momentum-dependent spin-splitting via Rashba SOC [28–30], restricting one’s ability to explore more intricate phases of matter.

One tantalizing possibility for shaping spin-orbital interactions lies in the engineering of the orbital degrees of freedom. Recent work in TMDs lays a promising path for such control [31–33]. More specifically, in bilayer moiré TMDs, the resulting superlattice potential can induce electronic flat bands with localized single-particle wavefunctions [34–36]. With one electron per moiré site, this setting realizes a spin-ful Hubbard model on the triangular superlattice [34–39]. However, at a filling of three electrons (or holes) per unit cell, the strong interparticle Coulomb repulsion at each moiré site can split the electronic charge density into a localized trimer—dubbed a Wigner molecule [31–33, 40–44].

In this work, we show that each Wigner molecule hosts a complex internal structure that leads to a rich family of spin-orbital Hamiltonians on the triangular lattice [Fig. 1(a)]. Our main results are threefold. First, we identify the low-energy Hilbert space for each Wigner molecule, via exact diagonalization (ED), as a degenerate four-dimensional space, characterized by spin,  $S = 1/2$ , and orbital angular momentum,  $L^z = \pm 1$ , that acts as

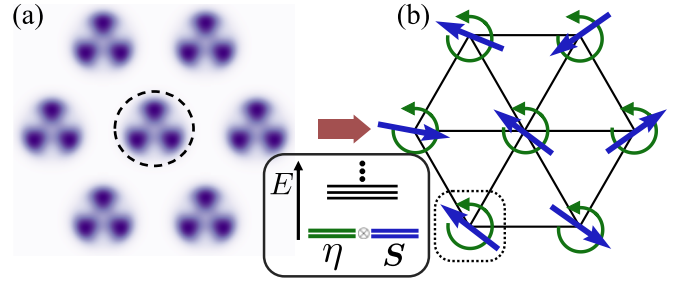


FIG. 1. (a) Charge density in a lattice of Wigner molecules. Each molecule (dotted circle) hosts three electrons localized at the vertices of an equilateral triangle, collectively forming a breathing kagome lattice. Inset: schematic energy spectrum showing that the ground state manifold is composed of four degenerate levels:  $(\eta^z, S^z) = (\pm 1, \pm 1/2)$ . (b) Schematic of the local spin and orbital degrees of freedom interacting on a triangular lattice.

a pseudospin. Second, we derive an effective spin-orbital Hamiltonian constrained by symmetries and compute the couplings in this Hamiltonian using perturbation theory, demonstrating that the magnetic frustration and anisotropy can be tuned via moiré superlattice length-scale and dielectric screening. Finally, using a combination of classical energy optimization and large-scale density matrix renormalization group (DMRG) calculation, we chart out the phase diagram of this Hamiltonian in the experimentally relevant regime. Specifically, we show that our spin-orbital model hosts a multitude of intriguing phases. These include not only classical multiferroic phases where orbital ferroelectricity intertwines with magnetic ordering of spins, but also intrinsically quantum phases such as a helical spin liquid characterized by spontaneous circulating spin-currents without any long-range magnetic order. Collectively, our results demonstrate how TMD moiré materials offer a powerful and versatile platform for generating and studying a wealth of new spin-orbital phenomena.

*Wigner molecule local Hilbert space.*— We begin by identifying the effective low-energy degrees of freedom of each Wigner molecule. To do so, we first review how Wigner molecules are formed in moiré TMD heterobilayers and  $\Gamma$ -valley homobilayers [45–49] (such as  $\text{WS}_2$ ). In these materials, the low-energy single particle physics is described by the moiré potential  $V(\mathbf{r}) = -2V_0 \left[ \sum_{\ell=1}^3 \cos(\mathbf{g}_\ell \cdot \mathbf{r} + \phi) \right]$ , where  $\mathbf{g}_\ell = \frac{4\pi}{\sqrt{3}a_M} \left( \sin \frac{2\pi\ell}{3}, \cos \frac{2\pi\ell}{3} \right)$  are reciprocal moiré lattice vectors and  $a_M$  is the moiré superlattice spacing. The minima of  $V(\mathbf{r})$  form a triangular lattice [Fig. 1(a)].

To understand the structure of the moiré confining potential, we expand  $V(\mathbf{r})$  on each site around its minima such that:

$$V(\mathbf{r} - \mathbf{r}_{\min}) = V_{\mathcal{O}}(\mathbf{r}) \approx \frac{1}{2}kr^2 + c_3 \sin(3\theta)r^3. \quad (1)$$

The confining potential is approximately harmonic (distorted by a weak trigonal moiré crystal field  $c_3$ ) with an intrinsic oscillator frequency  $\omega = \sqrt{k/m}$ , where  $k = 16\pi^2 V_0 \cos \phi / a_M^2$  and  $m$  is the band mass of the electron. Consequently, each moiré superlattice site can host localized electrons (or holes), with a confinement length-scale  $\xi_0 = (\hbar^2/mk)^{1/4} \lesssim a_M$ .

This single-particle description is strongly modified by interactions; intra-moiré-site Coulomb repulsion imbues the system with a charge gap at integer filling  $\nu$ , while at higher fillings [ $\nu \geq 2$ ], it modifies the structure of the localized wavefunctions. To this end, let us consider the following Hamiltonian for each moiré site:

$$\mathcal{H}_{\text{site}} = \sum_{i=1}^{\nu} \left[ \frac{\mathbf{p}_i^2}{2m} + V_{\mathcal{O}}(\mathbf{r}_i) \right] + \sum_{i < j} \mathcal{V}(\mathbf{r}_i - \mathbf{r}_j), \quad (2)$$

where  $\mathcal{V}(\mathbf{r}_i - \mathbf{r}_j) = \frac{e^2}{\varepsilon} \left( \frac{1}{|\mathbf{r}_i - \mathbf{r}_j|} - \frac{1}{\sqrt{|\mathbf{r}_i - \mathbf{r}_j|^2 + 2d_g^2}} \right)$  is the single-gate screened Coulomb interaction.  $d_g$  denotes the distance to the metal gate and  $\varepsilon = \varepsilon_0 \varepsilon_r$  quantifies the electric screening due to the dielectric substrate. The presence of strong Coulomb interactions within each site repels the electrons apart, reshaping the local charge density and forming a Wigner molecule [50–54], the zero-dimensional equivalent of a Wigner crystal. In contrast to the conventional  $\nu = 1$  Mott insulator [34, 55], the Wigner molecule can host additional orbital degrees of freedom, whose fluctuations enables novel quantum phases.

We focus on  $\nu = 3$ , where the local charge density takes a ‘three-lobed’ trimer form within a single molecule [31, 32], resulting in a breathing Kagome lattice [Fig. 1(a)] stabilized by the trigonal moiré crystal field. The simplest way to understand the low energy manifold of the Wigner molecule is by focusing on the non-interacting harmonic limit. In this limit, the single-particle energy eigenstates are given by  $E(n, l^z, s^z) =$

$(2n + |l^z| + 1)\hbar\omega$  [52], where each level has a two-fold degeneracy due to  $\text{SU}(2)_s$  spin-rotation symmetry of the spin-1/2 electron. The ground state manifold is then easy to obtain: the  $(n, l^z, s^z) = (0, 0, \pm 1/2)$  states are filled with two electrons, while the third electron has four degenerate options,  $(n, l^z, s^z) = (0, \pm 1, \pm 1/2)$ . These states have a total angular momentum of  $L^z = \sum_{i=1}^3 l_i^z = \pm 1$  and total spin of  $S^z = \sum_{i=1}^3 s_i^z = \pm 1/2$ . This picture is quite robust. First, the trigonal warping [ $c_3 \neq 0$  in Eq. 1] reduces the spatial symmetry from  $\text{U}(1)$  to  $\text{C}_{3v}$  so that  $L^z$  is only defined modulo 3, yet  $L^z = \pm 1$  remains a good quantum number. Second, the combination of time-reversal  $\mathcal{T}$  and  $\text{SU}(2)_s$  symmetry constrain eigenstates with  $L^z = \pm 1$  and  $S^z = \pm 1/2$  to remain degenerate *even when the electrons are interacting*. Therefore, below a critical interaction strength, the effective local Hilbert space remains exactly four-dimensional.

We confirm our intuitive expectation with an explicit ED computation of the spectrum of  $\mathcal{H}_{\text{site}}$  [31, 32]. Parameterizing the intra-site interaction strength by the ratio of the intra-unit-cell Coulomb repulsion,  $E_c = e^2/\varepsilon\xi_0$ , to the harmonic level spacing,  $\lambda = E_c/\hbar\omega$ , we find that for  $\lambda < \lambda_c \approx 4.5$ , the low-energy state-space remains four-dimensional. This space can be characterized as a tensor product of two spin-like degrees of freedom: (i) the total spin of the electrons, represented by  $\mathbf{S} = (S^x, S^y, S^z)$ , and (ii) a pseudospin-half degree of freedom capturing the total angular momentum  $L^z = \pm 1$ , represented by  $\boldsymbol{\eta} = (\eta^x, \eta^y, \eta^z)$ . Because the angular momentum is restricted to only two levels, the explicit mapping between  $\mathbf{L}$  and  $\boldsymbol{\eta}$  is given by  $L^z \rightarrow \eta^z$ ,  $\frac{1}{2}(L^+)^2 \rightarrow \eta^+$ , and  $\frac{1}{2}(L^-)^2 \rightarrow \eta^-$ . Crucially, this mapping shows that, while  $\eta^z$  remains odd under  $\mathcal{T}$ , the in-plane components of the orbital-pseudospin  $\boldsymbol{\eta}$ , namely  $\boldsymbol{\eta}_{\parallel} = (\eta^x, \eta^y)$  are *even* under  $\mathcal{T}$  and transform as a polar vector under rotations. This implies that the  $\boldsymbol{\eta}_{\parallel}$  behaves as an electrical polarization that couples linearly to in-plane electric field  $\mathbf{E}_{\parallel}$ , and its ordering leads to ferroelectricity.

To conclude this section, we note that for large intra-molecular Coulomb repulsion  $\lambda > \lambda_c$ , Hund’s rule prevails and the interacting ground state has higher total spin  $S = 3/2$  and  $L^z = 0$  [56]. In this limit,  $\text{SU}(2)_s$  symmetry constrains the triangular Wigner molecular lattice to realize a  $S = 3/2$  Heisenberg model, whose ground state is either the ferromagnet or the  $120^\circ$  antiferromagnet [57]. Therefore, in this work, we focus on  $\lambda < \lambda_c$ , where the spin and orbital degrees of freedom enable a plethora of frustrated magnetic and multiferroic phases, and turn to deriving the spin-orbital Hamiltonian that describes interacting Wigner molecules on a lattice.

*Effective spin-orbital model*— Having understood the low-energy manifold of each Wigner molecule, we can leverage our understanding of the system’s symmetries to constrain the form of the effective spin-orbital Hamiltonian. The system exhibits a  $\text{C}_{3v}$  point group symmetry

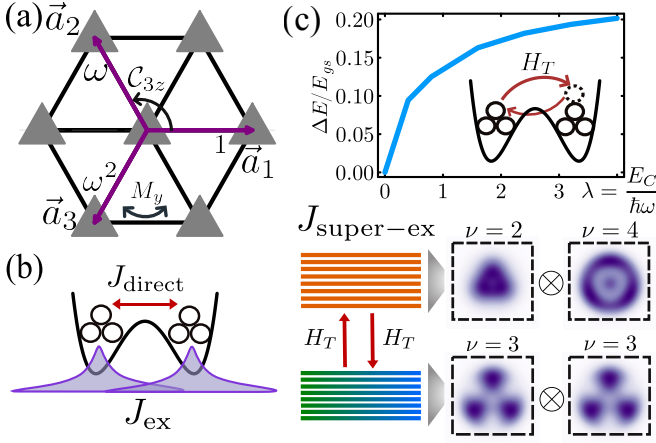


FIG. 2. (a) The point group symmetries of  $\mathcal{H}$  on the triangular lattice, with definitions of the lattice vectors  $\mathbf{a}_i$ , and bond-dependent phase factors  $\nu_{ij}$ . (b) Schematic of direct Coulomb repulsion  $J_{\text{direct}}$  between two Wigner molecules, and their exchange interaction  $J_{\text{ex}}$  from wave-function overlap. (c) Super-exchange  $J_{\text{super-ex}}$  arising from virtual tunneling of electrons to excited states with  $\nu \neq 3$ . Also shown are the charge gap  $\Delta E(\lambda)$  (upper panel) and the drastic modification of Wigner molecular shapes at  $\nu = 2, 4$  (lower panel).

[Fig. 2(a)], as well as time-reversal  $\mathcal{T}$  and  $\text{SU}(2)_s$  spin-rotation symmetry. Whereas spin-rotation symmetry constrains the spin-spin interactions to be Heisenberg-like, the reduced rotational symmetry of the orbital pseudospin  $\boldsymbol{\eta}$  allows for terms that either couple to the spin-Heisenberg term or appear as bilinears of  $\boldsymbol{\eta}$  operators only. Taken together, the most general symmetry-constrained Hamiltonian, focusing on nearest neighbor interactions, is given by [58]:

$$\mathcal{H} = \sum_{\langle ij \rangle} [(J_H + H_{zz}^s + H_{+-}^s + H_{++}^s + H_+) \mathbf{S}_i \cdot \mathbf{S}_j + (H_{zz}^o + H_{+-}^o + H_{++}^o)], \quad (3)$$

$$H_{zz}^\alpha = J_{zz}^\alpha \eta_i^z \eta_j^z$$

$$H_{+-}^\alpha = J_{+-}^\alpha e^{i\theta_{+-}^\alpha} \eta_i^+ \eta_j^- + h.c.$$

$$H_{++}^\alpha = J_{++}^\alpha (\nu_{ij} \eta_i^+ \eta_j^+ + h.c.)$$

$$H_+ = J_+ e^{i\theta_+} (\nu_{ij}^* \eta_i^+ + \nu_{ij} \eta_j^-) + h.c.$$

where  $\{J^\alpha\}$  denote the different couplings, superscript  $\alpha$  takes value  $s$  ( $o$ ) for spin-orbital (orbital only) terms, and  $\nu_{ij} = 1, \omega, \omega^2$  for bonds along lattice vectors  $\mathbf{a}_1, \mathbf{a}_2, \mathbf{a}_3$ , respectively. The general form of  $\mathcal{H}$  puts forth an expressive model that captures a wide variety of correlated spin-orbital physics.

Crucially, the expressibility of  $\mathcal{H}$  can be accessed in a wide range of materials, notably heterobilayer and homobilayer TMD stacks such as twisted bilayer  $\text{WS}_2$  [33], and  $\text{MoS}_2$  [59], heterobilayer  $\text{WSe}_2/\text{WS}_2$  and twisted double-bilayer  $\text{WSe}_2$  [60]. Given the tunability of these platforms, both in terms of the choice of van der Waals ma-

terials, but also twist angle, applied fields, and dielectric substrates, this expressibility can translate itself into the experimental exploration of a wealth of intricate orbital-magnetic phenomena. To highlight some of these features, we focus on the particular case of twisted bilayer  $\text{WS}_2$ , where a Wigner molecule lattice has been experimentally observed [33]; we now proceed to compute the various couplings for this material platform and study its phase diagram.

The different couplings  $J^\alpha$  are determined by three distinct physical effects: direct Coulomb repulsion, quantum mechanical exchange, and tunneling mediated super-exchange [55]. The direct Coulomb interaction naturally couples the orbital degrees of freedom; the asymmetric charge density profile at each site generates an electric field which directly couples to the charge density at nearby sites. Owing to the long-range nature of the Coulomb interaction, this effect is significant when the distance between neighboring sites is smaller than the gate-screening length,  $a_M \lesssim d_g$ . By contrast, the exchange interaction arises from the overlap of different Wigner molecules. Therefore, it is most significant for small  $a_M$  and  $\epsilon_r$ , where each Wigner molecule is larger. As  $a_M$  or  $\epsilon_r$  increase, super-exchange interactions, arising from virtual tunneling of electrons between adjacent Wigner molecules [Fig. 2(c)], start to dominate over exchange processes. In this regime, spin-spin interactions become antiferromagnetic, and the system becomes frustrated. Despite this simple description, the nature of the (super-)exchange interaction is qualitatively modified by the orbital degrees of freedom. Unlike the conventional Hubbard model [55], the shape of each Wigner molecule is drastically modified as the number of electrons at each site changes [Fig. 2(d)], inducing more complex matrix elements and orbital-spin interactions. This subtle interplay manifests itself into a rich phase diagram.

*Landscape of spin-orbital phenomena.*— We begin by considering classical phases captured by symmetry breaking patterns in  $\langle \mathbf{S} \rangle$  and/or  $\langle \boldsymbol{\eta} \rangle$ . To this end, we constrain  $\langle \boldsymbol{\eta} \rangle$  and  $2\langle \mathbf{S} \rangle$  to the unit sphere, and minimize  $\mathcal{H}[\langle \mathbf{S} \rangle, \langle \boldsymbol{\eta} \rangle]$  via manifold conjugate gradient descent [61–63], while considering enlarged unit cells to capture different translation symmetry breaking patterns [64]. We fix  $(\phi, d_g) = (45^\circ, 20 \text{ nm})$ , typical values for  $\text{WS}_2$  [33], and determine the minimum energy configuration of  $\langle \mathbf{S} \rangle, \langle \boldsymbol{\eta} \rangle$  as a function of  $(a_M, \epsilon_r)$ , which can be directly tuned by stacking and twisting of the TMD materials, and their dielectric environment, respectively. The resulting phase diagram is summarized in Fig. 3(a).

The simplest phase to understand is the spin-orbital ferromagnet (FM), which breaks both time-reversal  $\mathcal{T}$  and  $\text{SU}(2)_s$  spin rotation symmetries. This phase occurs when both the spin coupling  $J_H$  and the spin-orbital coupling  $J_{zz}^s$  are strongly ferromagnetic. The system is no longer highly frustrated, and both spin  $\mathbf{S}$  and orbital magnetic moment  $\eta^z$  can exhibit homogeneous, non-zero

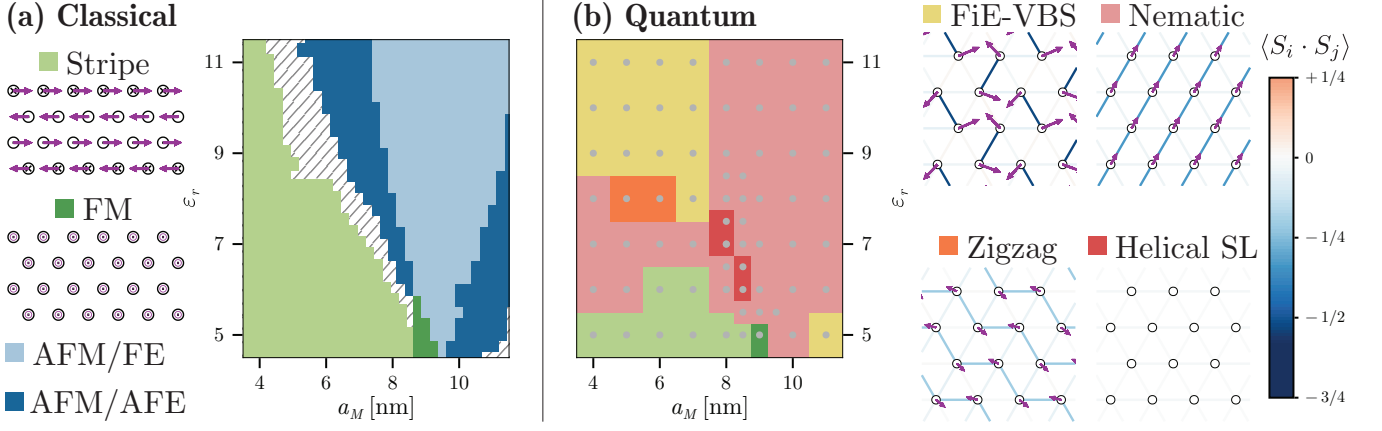


FIG. 3. (a) Phase diagram obtained by minimizing the energy over classical (pseudo)spin configurations at  $(\phi, d_g) = (45^\circ, 20 \text{ nm})$ . The two classical phases with quantum analogs are shown on the left. Our results are inconclusive in the cross-hatched region, which feature large unit cells suggesting high degeneracy or incommensurate order. (b) Corresponding quantum phase diagram from DMRG, showing the emergence of new, quantum-fluctuation induced phases depicted on the right. The in-plane orbital polarization  $\langle \eta_{\parallel} \rangle$  is shown by purple arrows, and spin-spin correlations on nearest neighbor bonds are indicated by color (blue implies antiferromagnetic).

expectation values. This offers a different path towards the realization of spin-orbital ferromagnetism that, unlike anomalous Hall phases in moiré TMDs [65–69], does not require the engineering of flat bands with significant Berry curvature.

When  $a_M$  is reduced,  $\mathcal{H}$  becomes dominated by the  $J_+$  term which linearly couples the in-plane orbital pseudospin  $\eta_{\parallel}$  to the Heisenberg spin-bilinear on bonds [Eq. 3]. The energy of a particular classical configuration can then be understood as follows. The pattern of spin-correlations on the bonds  $\langle ij \rangle$  generates a local field for  $\eta_{\parallel}$  at site  $i$ ; the energy of the state is dictated by the strength of the field which determines the orientation of  $\eta_{\parallel,i}$ . Owing to the  $C_{3v}$  symmetry of  $\mathcal{H}$ , the local field is exactly canceled when the system exhibits a ferromagnetic spin-ordering with uniform  $\langle S_i \cdot S_j \rangle$ —the lowest energy configuration must then exhibit a non-trivial pattern of spin correlations. Indeed, we observe the formation of a *stripe* pattern where both  $\langle \eta_{\parallel} \rangle$  and  $\langle S \rangle$  display an alternating collinear pattern, albeit with different periodicities, breaking both translation and rotational symmetries [Fig. 3(a)]. Notably, the coexistence of antiferroelectricity and magnetism implies that this stripe phase is multiferroic, suggesting a new avenue for designing materials with spintronic applications [30].

The rest of the classical phase diagram is either populated by an antiferromagnet, coexisting with in-plane ferroelectric (AFM/FE) or antiferroelectric (AFM/AFE) ordering (blue regions in Fig. 3(a), see SM for details [58]), or by ever more complex patterns of magnetism, characterized by large unit cells [hatched region in Fig. 3(a)]. The prevalence of several competing magnetic configurations in the classical phase diagram is a strong indication that quantum fluctuations play an im-

portant role in understanding the zero temperature phase diagram of  $\mathcal{H}$ .

To this end, we employ large-scale cylinder-iDMRG simulations with circumference  $L_y = 4 - 6$  to find the quantum ground state of  $\mathcal{H}$  [70]. The resulting phase diagram can be divided into three broad categories [Fig. 3(b)]. The first category are the phases already captured by the classical phase diagram; it includes both the spin-orbital ferromagnet and the stripe order, whose classical and quantum energy densities are nearly identical [58].

The second category includes point group symmetry breaking phases that are stabilized by quantum correlations [Fig. 3(b)]. These correlations give rise to either a Valence Bond Solid (VBS), where pairs of sites form spin singlets, or phases characterized by decoupled spin chains that realize one-dimensional Luttinger liquid physics [71].

The VBS phase emerges whenever  $\mathcal{H}$  is dominated by frustration-inducing antiferromagnetic interactions. Indeed, the location of this phase matches with the existence of competing classical configurations with large unit cells; quantum fluctuations drive the system to a VBS state with a non-collinear in-plane ordering for  $\eta_{\parallel}$  over a four-site unit cell. We dub this phase a ferrielectric valence bond solid (FiE-VBS) phase, as it features an in-plane electrical polarization owing to the non-zero net value of  $\langle \eta_{\parallel} \rangle$ .

The alternative pattern of  $C_{3v}$  symmetry breaking occurs when the spin degrees of freedom form one dimensional channels rather than singlets. This can either occur along a principal lattice direction [“Nematic” phase in Fig. 3(b)], or along more intricate paths [“Zigzag” phase in Fig. 3(b)]. These patterns of antiferromagnetic correlations occur on top of classical ordering of  $\eta_{\parallel}$ . This ob-



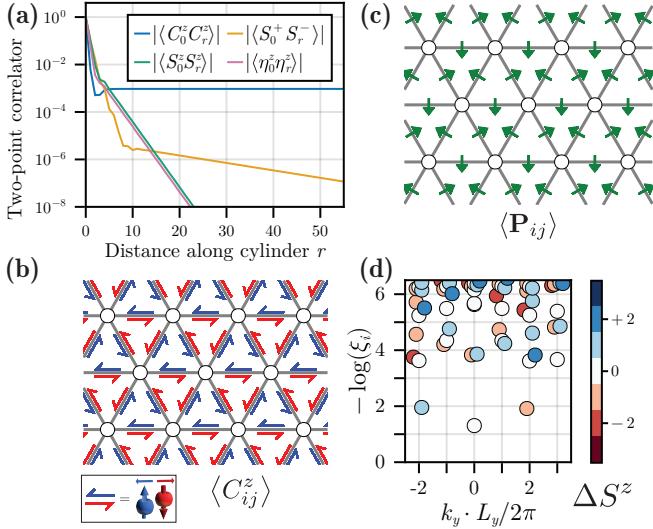


FIG. 4. Characterization of the HSL state found at  $(a_M, \varepsilon_r) = (8 \text{ nm}, 7)$ . (a) The exponential decay of the correlation functions  $\langle S_0^+ S_r^- \rangle$ ,  $\langle \eta_0^z \eta_r^z \rangle$ , and  $\langle S_0^z S_r^z \rangle$  indicates the lack of long-range order of either  $\vec{S}$  or  $\eta^z$ . By contrast,  $\langle C_0^z C_r^z \rangle$  quickly approaches a constant plateau, signifying the ordering of the spin-currents [75]. (b) Spin current pattern  $C_{ij}$ , which is of equal magnitude and sign on each bond. Since time-reversal is respected, along each bond, the spins of opposite orientation exhibit opposite currents of equal magnitude (blue and red arrows). (c) The  $C_{3v}$  symmetric spin current pattern,  $C_{ij}^z$ , induces a non-zero expectation value for the vector orbital polarization  $\mathbf{P}_{ij}$  (green arrows). (d) The spin- and momentum-resolved entanglement spectrum exhibits two low-lying modes of opposite momentum and spin, indicating spin-momentum locking.

servation offers a simple picture for origin of these states: the local electric polarization  $\langle \eta_{\parallel} \rangle_i$  modulates the spin-spin interaction along different bonds and enhances the antiferromagnetic coupling along certain paths, thereby inducing strong 1D correlations in a 2D system [72–74].

The final category exhibits no onsite order and preserves all point group symmetries—this is the hallmark of a spin liquid state. In the parameter regime exhibiting the greatest competition between different phases, we observe a state characterized by exponentially decaying correlations of single-site spin and orbital operators [Fig. 4(a)]. Remarkably, although the system lacks onsite order and preserves both  $C_{3v}$  and translation symmetries, it breaks the  $SU(2)_s$  spin-rotation symmetry. This is manifest in the spin-current operator  $\mathbf{C}_{ij} = \mathbf{S}_i \times \mathbf{S}_j$ ; in Fig. 4(c), we consider  $C_{ij}^z$  on nearest neighbor bonds  $\langle ij \rangle$ , showing it exhibits long-range order [Fig. 4(a)] [76]. This ordering pattern highlights an intriguing feature of this phase: even though  $SU(2)_s$  spin-rotation symmetry is broken, time reversal symmetry is preserved—for this reason we term this phase the Helical Spin Liquid (HSL).

We conclude with a few remarks about the HSL phase. First, although the phase lacks any onsite polarization,

the spin-current  $\mathbf{C}_{ij}$  on the bond  $\langle ij \rangle$  directly induces a bond electrical polarization  $\mathbf{P}_{ij}$ . One can understand the emergence of this effect from a simple symmetry argument. Given the vector  $\hat{a}_{ij}$  connecting sites  $i$  and  $j$ , both  $\mathbf{P}_{ij}$  and  $\hat{a}_{ij} \times \mathbf{C}_{ij}$  are  $\mathcal{T}$ -symmetric vectors; as a result, by symmetry, the Landau free energy has a term that is proportional to their dot product, linearly coupling the two. A non-zero expectation value of  $\mathbf{C}_{ij}$  then naturally generates a bond-polarization  $\mathbf{P}_{ij} \propto \hat{a}_{ij} \times \mathbf{C}_{ij}$ —indicating the emergence of an unconventional magnetoelectric effect [77]. We can make this analysis more concrete by constructing the microscopic orbital bilinear operator for the bond electrical polarization:  $\mathbf{P}_{ij} = (\eta_i^x \eta_j^y + \eta_i^y \eta_j^x, \eta_i^x \eta_j^x - \eta_i^y \eta_j^y)$ . Indeed,  $\langle \mathbf{P}_{ij} \rangle$  is non-zero in our ground state, while also clearly respecting the point group symmetric nature of this phase [Fig. 4(c)]. Second, although we only observe long-range ordering for the spin-current, the spin correlation  $\langle S_0^+ S_r^- \rangle$  exhibits a correlation length much larger than the other local correlation functions. While the exact source remains unclear, the phase of the correlator matches a periodicity of three sites, suggesting a small susceptibility to a  $120^\circ$  ordering that decreases with increasing bond dimension. Finally, the HSL exhibits a spontaneous, *interaction driven*, generation of spin-momentum locking in a  $SU(2)_s$  symmetric setting. This is in contrast to previous proposals for such locking (in time-reversal and  $SU(2)_s$  symmetric systems), where one either has a mean-field fermionic band picture describing a topological insulator [78], or higher-body, ring-exchange type interactions [79]. This locking is indicated by the half-system entanglement spectrum; the low-lying spectrum exhibits two modes with opposite momentum and spin [Fig. 4(d) blue and red].

*Conclusion and Outlook.*— Our work proposes moiré TMD materials as a novel platform for spin-orbital correlated matter. We demonstrate that such materials can naturally host lattices of Wigner molecules, and feature enhanced quantum fluctuations that lead to intriguing multiferroic and spin liquid phases. In particular, we find an elusive time-reversal symmetric helical spin liquid, which features spontaneous spin-currents, in a microscopically realizable spin-orbital Hamiltonian with only nearest neighbor interactions.

Our work opens the door to important future directions. One feature of our spin-orbital model is that  $\eta_{\parallel}$  is time-reversal even, leading it to couple directly to electric fields but not to magnetic fields. Therefore, one may independently use in-plane electric fields to polarize  $\eta$ , or in-plane magnetic fields to polarize spin  $\mathbf{S}$ , allowing for enhanced tunability and using dynamical electromagnetic responses [80–82] to distinguish different phases.

The tunability of the Wigner molecular platform extends beyond our studied spin-orbital model on multiple fronts. First, so far our exploration was restricted to the moiré lengthscale and electric permittivity. The plethora of tuning parameters available in such TMD materials

(including strain, stacking order and configuration, electric and magnetic fields, etc.) greatly extends the parameter ranges accessible in model Eq. 3. Second, while we focused on  $\Gamma$ -valley TMDs in this work, our proposal can naturally be adapted to  $K$ -valley TMDs which feature spin-valley locking, reducing  $SU(2)_s$  to  $U(1)_s$  [22, 83]. Finally, lattices of Wigner molecules can also be realized using bosonic degrees of freedom (such as moiré excitons [84]), enabling the study of role of quantum statistics in these correlated settings.

More broadly, our proposal motivates future studies of TMDs in a relatively less explored regime, requiring new tools to study and probe spin-orbital correlations. This could have important implications for realizing unconventional phases of quantum matter and developing novel materials for spintronic applications.

*Acknowledgments.*— We gratefully acknowledge helpful discussions with M. Bintz, S. Chern, M. Crommie, S. Divic, E. Khalaf, N. Verma, F. Wang, and M. P. Zaletel. This work used Bridges-2 at PSC through allocation PHY240241 from the Advanced Cyberinfrastructure Coordination Ecosystem: Services & Support (ACCESS) program[85], which is supported by U.S. National Science Foundation grants No. 2138259, No. 2138286, No. 2138307, No. 2137603, and No. 2138296. F. M. acknowledge support from the NSF through a grant for ITAMP at Harvard University.

- 
- [1] A. Kitaev, *Annals of Physics* **321**, 2–111 (2006).
  - [2] G. Jackeli and G. Khaliullin, *Phys. Rev. Lett.* **102**, 017205 (2009).
  - [3] J. Chaloupka, G. Jackeli, and G. Khaliullin, *Phys. Rev. Lett.* **105**, 027204 (2010).
  - [4] Y. Singh and P. Gegenwart, *Phys. Rev. B* **82**, 064412 (2010).
  - [5] R. Comin, G. Levy, B. Ludbrook, Z.-H. Zhu, C. N. Veenstra, J. A. Rosen, Y. Singh, P. Gegenwart, D. Stricker, J. N. Hancock, D. van der Marel, I. S. Elfimov, and A. Damascelli, *Phys. Rev. Lett.* **109**, 266406 (2012).
  - [6] Y. Li, G. Chen, W. Tong, L. Pi, J. Liu, Z. Yang, X. Wang, and Q. Zhang, *Phys. Rev. Lett.* **115**, 167203 (2015).
  - [7] Y.-D. Li, X. Wang, and G. Chen, *Phys. Rev. B* **94**, 035107 (2016).
  - [8] Z.-X. Luo, E. Lake, J.-W. Mei, and O. A. Starykh, *Phys. Rev. Lett.* **120**, 037204 (2018).
  - [9] K. I. Kugel' and D. I. Khomskii, *Soviet Physics Uspekhi* **25**, 231 (1982).
  - [10] E. Pavarini, E. Koch, and A. I. Lichtenstein, *Phys. Rev. Lett.* **101**, 266405 (2008).
  - [11] A. Koga, S. Nakauchi, and J. Nasu, *Phys. Rev. B* **97**, 094427 (2018).
  - [12] R. Iwazaki, H. Shinaoka, and S. Hoshino, *Phys. Rev. B* **108**, L241108 (2023).
  - [13] H. Takagi, T. Takayama, G. Jackeli, G. Khaliullin, and S. E. Nagler, *Nature Reviews Physics* **1**, 264 (2019).
  - [14] F. Matsukura, Y. Tokura, and H. Ohno, *Nature Nanotechnology* **10**, 209 (2015).
  - [15] R. Ramesh and S. Manipatruni, *Proceedings of the Royal Society A: Mathematical, Physical and Engineering Sciences* **477**, 20200942 (2021).
  - [16] J. F. Sierra, J. Fabian, R. K. Kawakami, S. Roche, and S. O. Valenzuela, *Nature Nanotechnology* **16**, 856 (2021).
  - [17] W.-Y. He, D. Goldhaber-Gordon, and K. T. Law, *Nature Communications* **11**, 1650 (2020).
  - [18] J. Zhu, J.-J. Su, and A. H. MacDonald, *Phys. Rev. Lett.* **125**, 227702 (2020), arXiv:2001.05084 [cond-mat.str-el].
  - [19] H. Polshyn, J. Zhu, M. A. Kumar, Y. Zhang, F. Yang, C. L. Tschirhart, M. Serlin, K. Watanabe, T. Taniguchi, A. H. MacDonald, and A. F. Young, *Nature (London)* **588**, 66 (2020), arXiv:2004.11353 [cond-mat.str-el].
  - [20] A. Abouelkomsan, E. J. Bergholtz, and S. Chatterjee, *Phys. Rev. Lett.* **133**, 026801 (2024).
  - [21] E. Y. Andrei, D. K. Efetov, P. Jarillo-Herrero, A. H. MacDonald, K. F. Mak, T. Senthil, E. Tutuc, A. Yazdani, and A. F. Young, *Nature Reviews Materials* **6**, 201 (2021).
  - [22] K. F. Mak and J. Shan, *Nature Nanotechnology* **17**, 686 (2022).
  - [23] K. P. Nuckolls and A. Yazdani, *Nature Reviews Materials* **9**, 460 (2024).
  - [24] Y. Zhang, R. Polski, A. Thomson, É. Lantagne-Hurtubise, C. Lewandowski, H. Zhou, K. Watanabe, T. Taniguchi, J. Alicea, and S. Nadj-Perge, *Nature* **613**, 268 (2023).
  - [25] Y. Zhang, G. Shavit, H. Ma, Y. Han, C. W. Siu, A. Mukherjee, K. Watanabe, T. Taniguchi, D. Hsieh, C. Lewandowski, *et al.*, *Nature* **641**, 625 (2025).
  - [26] C. L. Patterson, O. I. Sheekey, T. B. Arp, L. F. Holleis, J. M. Koh, Y. Choi, T. Xie, S. Xu, Y. Guo, H. Stoyanov, *et al.*, *Nature* **641**, 632 (2025).
  - [27] T. Wang, M. Vila, M. P. Zaletel, and S. Chatterjee, *Physical Review Letters* **132**, 116504 (2024).
  - [28] A. Manchon, H. C. Koo, J. Nitta, S. M. Frolov, and R. A. Duine, *Nature Materials* **14**, 871–882 (2015).
  - [29] G. Bihlmayer, P. Noël, D. V. Vyalikh, E. V. Chulkov, and A. Manchon, *Nature Reviews Physics* **4**, 642 (2022).
  - [30] S. Shi, X. Wang, Y. Zhao, and W. Zhao, *Materials Today Electronics* **6**, 100060 (2023).
  - [31] A. P. Reddy, T. Devakul, and L. Fu, *Phys. Rev. Lett.* **131**, 246501 (2023).
  - [32] C. Yannouleas and U. Landman, *Phys. Rev. B* **108**, L121411 (2023).
  - [33] H. Li, Z. Xiang, A. P. Reddy, T. Devakul, R. Sailus, R. Banerjee, T. Taniguchi, K. Watanabe, S. Tongay, A. Zettl, L. Fu, M. F. Crommie, and F. Wang, *Science* **385**, 86 (2024), <https://www.science.org/doi/pdf/10.1126/science.adk1348>.
  - [34] F. Wu, T. Lovorn, E. Tutuc, and A. H. MacDonald, *Phys. Rev. Lett.* **121**, 026402 (2018).
  - [35] H. Pan, F. Wu, and S. Das Sarma, *Phys. Rev. Res.* **2**, 033087 (2020).
  - [36] H. Pan, F. Wu, and S. Das Sarma, *Phys. Rev. B* **102**, 201104 (2020).
  - [37] K. Slagle and L. Fu, *Phys. Rev. B* **102**, 235423 (2020).
  - [38] N. Morales-Durán, P. Potasz, and A. H. MacDonald, *Phys. Rev. B* **107**, 235131 (2023).
  - [39] P. Potasz, N. Morales-Durán, N. C. Hu, and A. H. MacDonald, *Phys. Rev. B* **109**, 045144 (2024).
  - [40] D. Luo, A. P. Reddy, T. Devakul, and L. Fu, *arXiv e-prints*, arXiv:2303.08162 (2023), arXiv:2303.08162

- [cond-mat.str-el].
- [41] C. Yannouleas and U. Landman, *Phys. Rev. B* **109**, L121302 (2024).
  - [42] C. Yannouleas and U. Landman, *Phys. Rev. Lett.* **133**, 246502 (2024).
  - [43] X. Li, Y. Qian, W. Ren, Y. Xu, and J. Chen, arXiv preprint arXiv:2406.11134 (2024).
  - [44] Y. Li, Y.-J. Wang, and Z.-D. Song, *Chinese Physics B* **34**, 027303 (2025).
  - [45] M. Angeli and A. H. MacDonald, *Proceedings of the National Academy of Sciences* **118**, e2021826118 (2021), <https://www.pnas.org/doi/pdf/10.1073/pnas.2021826118>.
  - [46] Y. Zhang, T. Liu, and L. Fu, *Phys. Rev. B* **103**, 155142 (2021).
  - [47] H. C. P. Movva, T. Lovorn, B. Fallahazad, S. Larentis, K. Kim, T. Taniguchi, K. Watanabe, S. K. Banerjee, A. H. MacDonald, and E. Tutuc, *Phys. Rev. Lett.* **120**, 107703 (2018).
  - [48] G. Gatti, J. Issing, L. Rademaker, F. Margot, T. A. de Jong, S. J. van der Molen, J. Teyssier, T. K. Kim, M. D. Watson, C. Cacho, P. Dudin, J. Avila, K. C. Edwards, P. Paruch, N. Ubrig, I. Gutiérrez-Lezama, A. F. Morpurgo, A. Tamai, and F. Baumberger, *Phys. Rev. Lett.* **131**, 046401 (2023).
  - [49] M. Brzezińska, S. Grytsiuk, M. Rösner, M. Gibertini, and L. Rademaker, arXiv preprint arXiv:2404.07165 (2024).
  - [50] C. Yannouleas and U. Landman, *Phys. Rev. Lett.* **82**, 5325 (1999).
  - [51] R. Egger, W. Häusler, C. H. Mak, and H. Grabert, *Phys. Rev. Lett.* **82**, 3320 (1999).
  - [52] S. A. Mikhailov, *Phys. Rev. B* **65**, 115312 (2002).
  - [53] C. Ellenberger, T. Ihn, C. Yannouleas, U. Landman, K. Ensslin, D. Driscoll, and A. C. Gossard, *Phys. Rev. Lett.* **96**, 126806 (2006).
  - [54] S. Kalliakos, M. Rontani, V. Pellegrini, C. P. García, A. Pinczuk, G. Goldoni, E. Molinari, L. N. Pfeiffer, and K. W. West, *Nature Physics* **4**, 467 (2008).
  - [55] A. Auerbach, *Interacting electrons and quantum magnetism* (Springer Science & Business Media, 2012).
  - [56] D. J. Thouless, *Proceedings of the Physical Society* **86**, 893 (1965).
  - [57] A. Olariu, P. Mendels, F. Bert, L. K. Alexander, A. V. Mahajan, A. D. Hillier, and A. Amato, *Phys. Rev. B* **79**, 224401 (2009).
  - [58] For more details see the Supplementary Information.
  - [59] M. H. Naik, S. Kundu, I. Maity, and M. Jain, *Phys. Rev. B* **102**, 075413 (2020).
  - [60] B. A. Foutty, J. Yu, T. Devakul, C. R. Kometter, Y. Zhang, K. Watanabe, T. Taniguchi, L. Fu, and B. E. Feldman, *Nature Materials* **22**, 731 (2023).
  - [61] P. K. Mogensen, J. M. White, A. N. Riseth, T. Holy, M. Lubin, Christof, A. Noack, A. Levitt, B. Legat, C. Ortner, B. Johnson, C. Rackauckas, Y. Yu, K. Carlsson, D. Lin, A. Strouwen, J. Grawitter, T. Arakaki, B. Pasquier, abhro, T. R. Covert, R. Rock, M. Creel, cosio, J. Regier, D. Widmann, B. Kuhn, and A. Stukalov, *JuliaNLSolvers/Optim.jl: V1.13.2 (docs)*.
  - [62] A. Edelman, T. A. Arias, and S. T. Smith, *SIAM journal on Matrix Analysis and Applications* **20**, 303 (1998).
  - [63] P.-A. Absil, R. Mahony, and R. Sepulchre, in *Optimization Algorithms on Matrix Manifolds* (Princeton University Press, 2009).
  - [64] In practice, we allow for unit cells up to size 12. In most cases, we obtain better energetics for smaller unit cells.
  - [65] F. Wu, T. Lovorn, E. Tutuc, I. Martin, and A. H. MacDonald, *Phys. Rev. Lett.* **122**, 086402 (2019).
  - [66] T. Li, S. Jiang, B. Shen, Y. Zhang, L. Li, Z. Tao, T. Devakul, K. Watanabe, T. Taniguchi, L. Fu, J. Shan, and K. F. Mak, *Nature* **600**, 641 (2021).
  - [67] F. Xu, Z. Sun, T. Jia, C. Liu, C. Xu, C. Li, Y. Gu, K. Watanabe, T. Taniguchi, B. Tong, J. Jia, Z. Shi, S. Jiang, Y. Zhang, X. Liu, and T. Li, *Phys. Rev. X* **13**, 031037 (2023).
  - [68] Z. Tao, B. Shen, S. Jiang, T. Li, L. Li, L. Ma, W. Zhao, J. Hu, K. Pistunova, K. Watanabe, T. Taniguchi, T. F. Heinz, K. F. Mak, and J. Shan, *Phys. Rev. X* **14**, 011004 (2024).
  - [69] J. Cai, E. Anderson, C. Wang, X. Zhang, X. Liu, W. Holtzmann, Y. Zhang, F. Fan, T. Taniguchi, K. Watanabe, Y. Ran, T. Cao, L. Fu, D. Xiao, W. Yao, and X. Xu, *Nature* **622**, 63 (2023).
  - [70] J. Hauschild, J. Unfried, S. Anand, B. Andrews, M. Bintz, U. Borla, S. Divic, M. Drescher, J. Geiger, M. Hefel, K. Hémy, W. Kadow, J. Kemp, N. Kirchner, V. S. Liu, G. Möller, D. Parker, M. Rader, A. Romen, S. Scalet, L. Schoonderwoerd, M. Schulz, T. Soejima, P. Thoma, Y. Wu, P. Zechmann, L. Zweng, R. S. K. Mong, M. P. Zaletel, and F. Pollmann, *SciPost Phys. Codebases*, 41 (2024).
  - [71] T. Giamarchi, *Quantum physics in one dimension*, Vol. 121 (Clarendon press, 2003).
  - [72] W. Zheng, J. O. Fjærestad, R. R. P. Singh, R. H. McKenzie, and R. Coldea, *Phys. Rev. Lett.* **96**, 057201 (2006).
  - [73] Y. Hayashi and M. Ogata, *Journal of the Physical Society of Japan* **76**, 053705 (2007), <https://doi.org/10.1143/JPSJ.76.053705>.
  - [74] D. Heidarian, S. Sorella, and F. Becca, *Phys. Rev. B* **80**, 012404 (2009).
  - [75] Due to finite size and bond dimension effects, we observe a small rotation symmetry breaking in the in-plane components  $\langle \eta_{\parallel} \rangle$  [for more details see App. V A 4].
  - [76] Due to inherent constraints on DMRG, we need to add a small pinning field to see this order in correlators of the spin-current, see [58].
  - [77] H. Katsura, N. Nagaosa, and A. V. Balatsky, *Phys. Rev. Lett.* **95**, 057205 (2005).
  - [78] S. Raghu, X.-L. Qi, C. Honerkamp, and S.-C. Zhang, *Phys. Rev. Lett.* **100**, 156401 (2008).
  - [79] A. Läuchli, J. C. Domenge, C. Lhuillier, P. Sindzingre, and M. Troyer, *Phys. Rev. Lett.* **95**, 137206 (2005).
  - [80] S. Chatterjee, J. F. Rodriguez-Nieva, and E. Demler, *Phys. Rev. B* **99**, 104425 (2019).
  - [81] R. Sahay, S. Hsieh, E. Parsonnet, L. W. Martin, R. Ramesh, N. Y. Yao, and S. Chatterjee, arXiv preprint arXiv:2111.09315 (2021).
  - [82] F. Machado, E. A. Demler, N. Y. Yao, and S. Chatterjee, *Phys. Rev. Lett.* **131**, 070801 (2023).
  - [83] D. Xiao, G.-B. Liu, W. Feng, X. Xu, and W. Yao, *Physical review letters* **108**, 196802 (2012).
  - [84] Y. Meng, L. Ma, L. Yan, A. Khalifa, D. Chen, S. Zhang, R. Banerjee, T. Taniguchi, K. Watanabe, S. A. Tongay, B. Hunt, S. Lin, W. Yao, Y. Cui, S. Chatterjee, and S. Shi, *Nature Photonics*, in press (2025).
  - [85] T. J. Boerner, S. Deems, T. R. Furlani, S. L. Knuth, and J. Towns, in *Practice and Experience in Advanced Research Computing 2023: Computing for the Common Good*, PEARC '23 (Association for Computing Machinery, New York, NY, USA, 2023) p. 173–176.

- [86] I. S. Gradshteyn and I. M. Ryzhik, *Table of integrals, series, and products*, seventh ed. (Elsevier/Academic Press, Amsterdam, 2007) pp. xlviii+1171.
- [87] J. López-Bonilla and G. Ovando, Bull. Irish Math. Soc.(44) **61** (2000).
- [88] I. Guseinov, B. Mamedov, and A. Ekenoğlu, [Computer Physics Communications](#) **175**, 226 (2006).
- [89] R. Sahay, S. Divic, D. E. Parker, T. Soejima, S. Anand, J. Hauschild, M. Aidelsburger, A. Vishwanath, S. Chatterjee, N. Y. Yao, and M. P. Zaletel, [Phys. Rev. B](#) **110**, 195126 (2024).



## Supplemental Material: Spin-orbital magnetism in moiré Wigner molecules

### I. EXACT DIAGONALIZATION ON A SINGLE MOIRÉ SITE

For the sake of completeness, we review the 2D harmonic oscillator which we use to form our single-particle basis in order to obtain the spectrum of  $N$  interacting electrons. The expansion of the moiré potential up to order  $r^6$  and ignoring the constant shift is:

$$V_O(\mathbf{r}) = 8V_0\pi^2 \cos(\phi) \left(\frac{r}{a_M}\right)^2 + \frac{16V_0\pi^3}{3\sqrt{3}} \sin(\phi) \sin(3\theta) \left(\frac{r}{a_M}\right)^3 - \frac{8V_0\pi^4}{3} \cos(\phi) \left(\frac{r}{a_M}\right)^4 \\ - \frac{16V_0\pi^5}{9\sqrt{3}} \sin(\phi) \sin(3\theta) \left(\frac{r}{a_M}\right)^5 + \frac{16V_0\pi^6}{405} \cos(\phi)(10 - \cos(6\theta)) \left(\frac{r}{a_M}\right)^6. \quad (S1.1)$$

Truncating to the second order, we get the harmonic oscillator problem with the Hamiltonian,

$$H = \frac{p^2}{2m} + \frac{1}{2}kr^2, \quad (S1.2)$$

where  $k = 16V_0\pi^2 \cos(\phi)/a_M^2$ . In order to make use of the U(1) symmetry of the Hamiltonian, we define creation and annihilation operators that make the symmetry manifest,

$$a_{\pm} = \frac{1}{2} \left[ \frac{x \mp iy}{\xi} + \frac{\xi}{\hbar} (p_x \mp ip_y) \right], \quad (S1.3)$$

where we define the characteristic length scale of the harmonic oscillator by  $\xi \equiv (\hbar^2/mk)^{1/4}$ . In terms of the creation and annihilation operators, the Hamiltonian becomes,

$$H = \hbar\omega(a_+^\dagger a_+ + a_-^\dagger a_- + 1) \quad (S1.4)$$

The energy spectrum is simply,  $E = \hbar\omega(n_+ + n_- + 1)$ , where  $n_{\pm} \in \{0, 1, 2, \dots\}$ , and the eigenstates are,

$$|n_+ n_- \rangle = \frac{(a_+^\dagger)^{n_+} (a_-^\dagger)^{n_-}}{\sqrt{n_+! n_-!}} |00\rangle \quad (S1.5)$$

These states are also eigenstates of the  $z$ -component of orbital angular momentum operator,  $L^z = xp_y - yp_x = a_+^\dagger a_+ - a_-^\dagger a_-$  with eigenvalues  $l = n_+ - n_-$ . So an equivalent label of the states is given by  $n, l$  where  $n \equiv \min(n_+, n_-)$ . The real space wave functions are the Fock-Darwin orbitals, and they are given by,

$$\psi_{n,l,s}(\mathbf{r}) = \frac{(-1)^n}{\xi} \sqrt{\frac{n!}{\pi(n+|l|)!}} e^{il\theta} (r/\xi)^{|l|} L_n^{|l|}((r/\xi)^2) e^{-\frac{(r/\xi)^2}{2}} \chi_s, \quad (S1.6)$$

where  $s$  denotes spin up or down.

In our exact diagonalization (ED) calculations, we use these single-particle orbitals to form a basis made of single Slater determinants (SSD) for the states of  $N$  electrons. so that a general many-body wave function is a linear combination of these states as,

$$\Phi_m(\mathbf{r}_1, \dots, \mathbf{r}_N) = \sum_i c_i^m \Psi_{SSD}^i(\mathbf{r}_1, \dots, \mathbf{r}_N) \quad (S1.7)$$

We then write the Hamiltonian operator as a matrix which we diagonalize to get the ground state and the first few excited states. If we define  $n \equiv n_+ + n_- + 1$  as a collective label for the single-particle orbitals, we keep up to  $n_{max} = 8$  as a cutoff which translates to 36 spin orbitals. The number of many-body states in the basis set is 1028790, 59640, 2556 for  $N = 4$ ,  $N = 3$ ,  $N = 2$ , respectively. We check the convergence by calculating the percent error in the ground state energy as the basis cutoff is changed. We find  $(E_{28} - E_{36})/E_{28} \approx 0.1\%$  which indicates that the basis cutoff of 36 spin orbitals is justified. We also make use of the symmetry of the system which makes the Hamiltonian block-diagonal in the total  $S^z$  and  $L^z \bmod 3$ .

## II. COULOMB MATRIX ELEMENTS

### A. Direct term

Here, we present the derivation of the Coulomb matrix elements which are decomposed into direct and exchange terms. We closely follow the method of [S31], and we generalize it to the general situation for our purposes which includes intersite interaction with gate screening. The Coulomb energy between two electrons at two points (the two points are separated along the  $x$  axis by  $a$ ) is given by

$$U(\mathbf{r}) = \frac{2\pi e^2}{\epsilon} \int \frac{d^2 q}{(2\pi)^2} U(\mathbf{q}) e^{i\mathbf{q}\cdot\mathbf{r}} e^{iq_x a} \quad (\text{S2.1})$$

where we use the single gate screened Coulomb interaction

$$U(\mathbf{q}) = \frac{1 - e^{-2qd}}{q} \quad (\text{S2.2})$$

We define the complex momentum measured in units of  $\xi$  as

$$\tilde{q} = \frac{q_x + iq_y}{2} \quad (\text{S2.3})$$

The Coulomb matrix element is

$$U_{ijkl} = \int \frac{d^2 q}{(2\pi)^2} \frac{1 - e^{-2qd}}{q} e^{iqa \cos \phi} \langle n_{+i} n_{-i}, n_{+j} n_{-j} | e^{i\mathbf{q}\cdot(\mathbf{r}_1 - \mathbf{r}_2)} | n_{+k} n_{-k}, n_{+l} n_{-l} \rangle \quad (\text{S2.4})$$

In terms of  $\tilde{q}$ , we have

$$U_{ijkl} = 2E_C \int \frac{d^2 \tilde{q}}{2\pi} U(\tilde{q}, \phi) \langle n_{+i} | e^{i(\tilde{q}a_+^\dagger + \tilde{q}^* a_+)} | n_{+k} \rangle \langle n_{-i} | e^{i(\tilde{q}a_- + \tilde{q}^* a_-^\dagger)} | n_{-k} \rangle \langle n_{+j} | e^{-i(\tilde{q}a_+^\dagger + \tilde{q}^* a_+)} | n_{+l} \rangle \langle n_{-j} | e^{-i(\tilde{q}a_- + \tilde{q}^* a_-^\dagger)} | n_{-l} \rangle \quad (\text{S2.5})$$

where  $U(\tilde{q}, \phi) = \frac{1 - e^{-4\tilde{q}d}}{\tilde{q}}$ . The matrix element becomes

$$\begin{aligned} U_{ijkl} &= 2E_C (-1)^{N_j + N_k} i^{\Delta N} (n_{i+}! n_{j+}! n_{k+}! n_{l+}! n_{i-}! n_{j-}! n_{k-}! n_{l-}!)^{1/2} \int \frac{d^2 \tilde{q}}{2\pi} U(\tilde{q}, \phi) e^{-2\tilde{q}^2} e^{i\Delta l \phi} \\ &\times \left( \sum_{\alpha=0}^{\min(n_{i+}, n_{k+})} \frac{(-1)^\alpha |\tilde{q}|^{n_{i+} + n_{k+} - 2\alpha}}{\alpha! (n_{i+} - \alpha)! (n_{k+} - \alpha)!} \right) \left( \sum_{\beta=0}^{\min(n_{i-}, n_{k-})} \frac{(-1)^\beta |\tilde{q}|^{n_{i-} + n_{k-} - 2\beta}}{\beta! (n_{i-} - \beta)! (n_{k-} - \beta)!} \right) \\ &\times \left( \sum_{\gamma=0}^{\min(n_{j+}, n_{l+})} \frac{(-1)^\gamma |\tilde{q}|^{n_{j+} + n_{l+} - 2\gamma}}{\gamma! (n_{j+} - \gamma)! (n_{l+} - \gamma)!} \right) \left( \sum_{\eta=0}^{\min(n_{j-}, n_{l-})} \frac{(-1)^\eta |\tilde{q}|^{n_{j-} + n_{l-} - 2\eta}}{\eta! (n_{j-} - \eta)! (n_{l-} - \eta)!} \right) \\ &= 2E_C (-1)^{N_j + N_k} i^{\Delta N} (n_{i+}! n_{j+}! n_{k+}! n_{l+}! n_{i-}! n_{j-}! n_{k-}! n_{l-}!)^{1/2} \\ &\times \sum_{\alpha=0}^{\min(n_{i+}, n_{k+})} \frac{(-1)^\alpha}{\alpha! (n_{i+} - \alpha)! (n_{k+} - \alpha)!} \sum_{\beta=0}^{\min(n_{i-}, n_{k-})} \frac{(-1)^\beta}{\beta! (n_{i-} - \beta)! (n_{k-} - \beta)!} \\ &\times \sum_{\gamma=0}^{\min(n_{j+}, n_{l+})} \frac{(-1)^\gamma}{\gamma! (n_{j+} - \gamma)! (n_{l+} - \gamma)!} \sum_{\eta=0}^{\min(n_{j-}, n_{l-})} \frac{(-1)^\eta}{\eta! (n_{j-} - \eta)! (n_{l-} - \eta)!} I_q(p) \end{aligned} \quad (\text{S2.6})$$

$$I_q(p) = \int \frac{d^2 \tilde{q}}{2\pi} e^{-2\tilde{q}^2} \tilde{q}^{p-1} (1 - e^{-4\tilde{q}d}) e^{i\Delta l \phi} e^{2i\tilde{q}a \cos \phi} \quad (\text{S2.7})$$

A special case is  $a = 0$  which corresponds to the intrasite Coulomb interaction with screening. The integral becomes

$$I(a = 0) = \int_0^\infty d\tilde{q} e^{-2\tilde{q}^2} \tilde{q}^p (1 - e^{-4\tilde{q}d}) = 2^{\frac{-3}{2}} 2^{\frac{-p}{2}} \left[ \Gamma\left(\frac{p+1}{2}\right) - \Gamma(p+1) U\left(\frac{p+1}{2}, \frac{1}{2}, 2d^2\right) \right] \quad (\text{S2.8})$$

Another special case is the case of intersite interaction but with no screening so  $d = 0$ . We can do the  $\phi$  integral first to get

$$I_\phi = \frac{1}{2\pi} \int_0^{2\pi} d\phi e^{i\Delta l \phi} e^{2i\tilde{q}a \cos \phi} = i^{\Delta l} J_{\Delta l}(2\tilde{q}a) \quad \text{for } \Delta l > 0 \quad (\text{S2.9})$$

For  $\Delta l < 0$ , we have  $I_\phi = i^{3\Delta l} J_{|\Delta l|}(2\tilde{q}a)$ . This integral is found in [S86] Then we have

$$I(d=0) = i^{\Delta l \Theta'(\Delta l)} \int_0^\infty d\tilde{q} e^{-2\tilde{q}^2} \tilde{q}^p J_{|\Delta l|}(2\tilde{q}a) = i^{\Delta l \Theta'(\Delta l)} 2^{-\frac{3}{2}} 2^{-\frac{p+|\Delta l|}{2}} \frac{\Gamma\left(\frac{p+|\Delta l|+1}{2}\right)}{\Gamma(|\Delta l|+1)} a^{|\Delta l|} M\left(\frac{p+|\Delta l|+1}{2}, |\Delta l|+1, -\frac{a^2}{2}\right) \quad (\text{S2.10})$$

This integral is found in [S86]

The most general case does not have a closed form. So the remaining integral is when  $d \neq 0$ ,  $a \neq 0$ .

$$I_{d,a} = - \int \frac{d^2 \tilde{q}}{2\pi} e^{-2\tilde{q}^2} \tilde{q}^{p-1} e^{-4\tilde{q}d} e^{i\Delta l \phi} e^{2i\tilde{q}a \cos \phi} \quad (\text{S2.11})$$

First we do the radial integral

$$I_\phi = \int_0^\infty d\tilde{q} e^{-2\tilde{q}^2} \tilde{q}^p e^{-4\tilde{q}d} e^{2i\tilde{q}a \cos \phi} = 2^{-\frac{3}{2}} 2^{-\frac{3p}{2}} \Gamma(p+1) U\left(\frac{1+p}{2}, \frac{1}{2}, \frac{(2d - ia \cos \phi)^2}{2}\right) \quad (\text{S2.12})$$

Then  $I_{d,a}$  becomes

$$I_{d,a} = -2^{-\frac{3}{2}} 2^{-\frac{3p}{2}} \Gamma(p+1) \int_0^{2\pi} \frac{d\phi}{2\pi} e^{i\Delta l \phi} U\left(\frac{1+p}{2}, \frac{1}{2}, \frac{(2d - ia \cos \phi)^2}{2}\right) \quad (\text{S2.13})$$

## B. Exchange term

Our previous calculations only capture the direct part of the intersite Coulomb interactions. Now we will extend it. First, recall this is the Coulomb interaction operator

$$U(\mathbf{r}_1 - \mathbf{r}_2) = \frac{e^2}{\epsilon} \int \frac{d^2 q}{2\pi} U(\mathbf{q}) e^{i\mathbf{q} \cdot (\mathbf{r}_1 - \mathbf{r}_2)} \quad (\text{S2.14})$$

We will compute the matrix element of this operator in the basis  $(n_x, n_y)$  of the harmonic oscillator which takes the form,

$$U_{ijkl} = E_C \int \frac{d^2 q}{2\pi} U(\mathbf{q}) \int d^2 r_1 d^2 r_2 \psi_{n_{xi}, n_{yi}}(\mathbf{r}_1) \psi_{n_{xj}, n_{yj}}(\mathbf{r}_2 - a) e^{i\mathbf{q} \cdot (\mathbf{r}_1 - \mathbf{r}_2)} \psi_{n_{xk}, n_{yk}}(\mathbf{r}_1 - a) \psi_{n_{xl}, n_{yl}}(\mathbf{r}_2) \quad (\text{S2.15})$$

Note that we dropped the complex conjugate because the basis functions are real. The central object of this calculation is the form factor  $F$  that is

$$F_1(\mathbf{q}) = \int d^2 r_1 \psi_{n_{xi}, n_{yi}}(\mathbf{r}_1) e^{i\mathbf{q} \cdot \mathbf{r}_1} \psi_{n_{xk}, n_{yk}}(\mathbf{r}_1 - a) \quad (\text{S2.16})$$

We redefine the position and the momentum in terms of dimensionless variables.  $\tilde{\mathbf{r}} = \mathbf{r}/\xi_0$ ,  $\tilde{\mathbf{q}} = \xi_0 \mathbf{q}$ . so from now on all momenta and position are to be measured with respect to the length scale  $\xi_0$ .

$$F_1(\mathbf{q}) = \int_{-\infty}^\infty dx \psi_{n_{xi}}(x) e^{iq_x x} \psi_{n_{xk}}(x - a) \int_{-\infty}^\infty dy \psi_{n_{yi}}(y) e^{iq_y y} \psi_{n_{yk}}(y) \quad (\text{S2.17})$$

The  $y$  integral can be evaluated simply per ref [S87]

$$\langle m | e^{-\gamma y} | n \rangle = \sqrt{2^{n-m} \frac{n!}{m!}} (-\gamma)^{m-n} e^{\frac{\gamma^2}{4}} L_n^{m-n} \left( \frac{-\gamma^2}{2} \right) \quad (\text{S2.18})$$

Assuming  $m > n$  without loss of generality as the matrix element is symmetric. So in order to apply this formula to our case, we have  $m_1 = \max(n_{yi}, n_{yk})$  and  $m_2 = \max(n_{yl}, n_{yj})$ . We also assume without any loss of generality that  $n_{yi} > n_{yk}$  and  $n_{yj} > n_{yl}$ . This leads to the following for the  $y$  integral,

$$I_y = \sqrt{2^{n_{yk}-n_{yi}} \frac{n_{yk}!}{n_{yi}!}} (iq_y)^{n_{yi}-n_{yk}} e^{-\frac{q_y^2}{4}} L_{n_{yk}}^{n_{yi}-n_{yk}} \left( \frac{q_y^2}{2} \right) \quad (\text{S2.19})$$

Where the associated Laguerre polynomial is,

$$L_n^q(x) = \sum_{k=0}^n \frac{(-1)^k (n+q)! x^k}{k! (k+q)! (n-k)!} \quad (\text{S2.20})$$

We can then write  $I_y$  as,

$$I_y = \sqrt{2^{n_{yk}-n_{yi}} n_{yk}! n_{yi}!} (i)^{n_{yi}-n_{yk}} e^{-\frac{q_y^2}{4}} \sum_{p=0}^{n_{yk}} \frac{(-1)^p q_y^{2p+n_{yi}-n_{yk}}}{2^p p! (p+n_{yi}-n_{yk})! (n_{yk}-p)!} \quad (\text{S2.21})$$

For the  $x$  integral we use the result in ref [S88]

$$I_x = \frac{(-1)^{n_{xi}+n_{xk}} e^{\frac{iq_x a}{2}} e^{-\frac{q_x^2 - a^2}{4}}}{\sqrt{2^{n_{xi}+n_{xk}} n_{xi}! n_{xk}!}} \sum_{i=0}^{n_{xi}} \sum_{j=0}^{n_{xk}} \sum_{k=0}^{\lfloor \frac{n}{2} \rfloor} \binom{n_{xi}}{i} \binom{n_{xk}}{j} H_{n_{xi}-i} \left( \frac{-a}{2} \right) H_{n_{xk}-j} \left( \frac{a}{2} \right) \frac{n! (-iq_x)^{n-2k}}{(n-2k)! k!} \quad (\text{S2.22})$$

where  $n = i + j$ .

The  $\mathbf{r}_2$  integral is similar with the replacements of  $i\mathbf{q} \rightarrow -i\mathbf{q}$ ,  $n_{xi} \rightarrow n_{xl}$ ,  $n_{xk} \rightarrow n_{xj}$ .

Now we are left with the  $\mathbf{q}$  integral. We collect all the terms depending on  $\mathbf{q}$ ,

$$I_q = \int \frac{d^2 q}{2\pi} U(\mathbf{q}) e^{-q^2/2} (-iq_x)^{n_1-2k_1} (iq_x)^{n_2-2k_2} q_y^{2p_1+2p_2+n_{yi}+n_{yj}-n_{yk}-n_{yl}} \quad (\text{S2.23})$$

then the only terms depending on  $\mathbf{q}$  gives,

$$\begin{aligned} I_q &= \int \frac{d^2 q}{2\pi} U(\mathbf{q}) e^{-q^2/2} q_x^{n_1+n_2-2k_1-2k_2} q_y^{2p_1+2p_2+n_{yi}+n_{yj}-n_{yk}-n_{yl}} \\ &= \frac{1}{2\pi} \int_0^{2\pi} d\phi \int_0^\infty dq U(q) e^{-q^2/2} q^{n_1+n_2-2k_1-2k_2+2p_1+2p_2+n_{yi}+n_{yj}-n_{yk}-n_{yl}} \cos \phi^{n_1+n_2-2k_1-2k_2} \sin \phi^{2p_1+2p_2+n_{yi}+n_{yj}-n_{yk}-n_{yl}} \end{aligned} \quad (\text{S2.24})$$

Note that this integral and the whole matrix element vanishes if  $n_{yi} + n_{yj} - n_{yk} - n_{yl}$  is odd. Let  $p = 2p_1 + 2p_2 + n_{yi} + n_{yj} - n_{yk} - n_{yl} + n_1 + n_2 - 2k_1 - 2k_2$ ,  $p_x = n_1 + n_2 - 2k_1 - 2k_2$ ,  $p_y = 2p_1 + 2p_2 + n_{yi} + n_{yj} - n_{yk} - n_{yl}$ . With that in mind, the result of the integral becomes,

$$I_q = \frac{(1 + (-1)^{p_x}) 2\Gamma\left(\frac{p_x+1}{2}\right) \Gamma\left(\frac{p_y+1}{2}\right)}{4\pi\Gamma\left(\frac{2+p}{2}\right)} 2^{-\frac{p}{2}} \left[ 2^{-\frac{1}{2}+p}\Gamma\left(\frac{p+1}{2}\right) - d\Gamma(p+1)U\left(p+\frac{1}{2}, \frac{3}{2}, 2d^2\right) \right] \quad (\text{S2.25})$$

Finally, we can write down the final result for the matrix element.

$$\begin{aligned} U_{ijkl} &= \mathcal{N} \sum_{i_1, i_2, j_1, j_2} \sum_{k_1, k_2, p_1, p_2} \binom{n_{xi}}{i_1} \binom{n_{xl}}{i_2} \binom{n_{xk}}{j_1} \binom{n_{xj}}{j_2} H_{n_{xi}-i_1} \left( \frac{-a}{2} \right) H_{n_{xl}-i_2} \left( \frac{-a}{2} \right) H_{n_{xk}-j_1} \left( \frac{a}{2} \right) H_{n_{xj}-j_2} \left( \frac{a}{2} \right) \\ &\quad \frac{(-i)^{i_1+j_1-2k_1} (i_1+j_1)! i^{i_2+j_2-2k_2} (i_2+j_2)!}{(i_1+j_1-2k_1)! k_1! (i_2+j_2-2k_2)! k_2!} \frac{(-1)^{p_1}}{2^{p_1} p_1! (p_1+n_{yi}-n_{yk})! (n_{yk}-p_1)!} \\ &\quad \frac{(-1)^{p_2}}{2^{p_2} p_2! (p_2+n_{yj}-n_{yl})! (n_{yl}-p_2)!} I_q(k_1, k_2, p_1, p_2), \end{aligned} \quad (\text{S2.26})$$

$$\mathcal{N} = \frac{E_C}{4\pi} \frac{i^{n_{y1}} (-i)^{n_{y2}} \sqrt{2^{-N_y} n_{yk}! n_{yi}! n_{yj}! n_{yl}!}}{\sqrt{2^{N_x} n_{xk}! n_{xi}! n_{xj}! n_{xl}!}} e^{-\frac{a^2}{2}}$$



### III. THE EFFECTIVE SPIN-ORBITAL HAMILTONIAN

#### A. Symmetry

Here we list the symmetries of the Hamiltonian and how they act on the pseudospin  $\boldsymbol{\eta}$  and the spin  $\boldsymbol{S}$  degrees of freedom.

- $SU(2)_s$  spin rotation symmetry acting on  $\boldsymbol{S}$  as  $\boldsymbol{S} \rightarrow U^\dagger(\hat{\boldsymbol{n}}, \theta) \boldsymbol{S} U(\hat{\boldsymbol{n}}, \theta)$ , with  $U(\hat{\boldsymbol{n}}, \theta) = e^{-i\theta \hat{\boldsymbol{n}} \cdot \boldsymbol{S} / \hbar}$
- Time reversal:  $\boldsymbol{S}_i \rightarrow -\boldsymbol{S}_i$ ,  $\eta_i^z \rightarrow -\eta_i^z$ ,  $\eta_i^+ \rightarrow \eta_i^-$ .
- $C_{3z}$  about a lattice site:  $\boldsymbol{S}_{\boldsymbol{r}_i} \rightarrow U^\dagger(\hat{z}, \frac{2\pi}{3}) \boldsymbol{S}_{O_3 \boldsymbol{r}_i} U(\hat{z}, \frac{2\pi}{3})$ ,  $\eta_{\boldsymbol{r}_i}^+ \rightarrow \omega^2 \eta_{O_3 \boldsymbol{r}_i}^+$ , where  $O_3$  is the 2D rotation matrix by  $2\pi/3$ , and  $\omega \equiv e^{2\pi i/3}$ .
- A mirror about the  $yz$  plane:  $\boldsymbol{S}_{\boldsymbol{r}_i} \rightarrow (S_{M_y \boldsymbol{r}_i}^x, -S_{M_y \boldsymbol{r}_i}^y, -S_{M_y \boldsymbol{r}_i}^z)$ ,  $\eta_{\boldsymbol{r}_i}^+ \rightarrow \eta_{M_y \boldsymbol{r}_i}^-$ , where  $M_y$  is the reflection operator.

#### B. Calculation of the Couplings

We go into the details of how the various  $J^\alpha$  couplings in the effective spin model (equation (4) of the main text) are determined using perturbation theory. We consider two nearest neighbor sites in the triangular lattice  $(i, j)$  that are related to each other by reflection; the remaining couplings can be obtained from symmetry. The Hilbert space of the degenerate ground state manifold is 16-dimensional. It is spanned by the superposition of states  $|\Psi_{is\eta}\rangle \otimes |\Psi_{js'\eta'}\rangle$  that forms an  $S = 0$  singlet and an  $S = 1$  triplet. Due to the  $SU(2)_s$  symmetry, the Hamiltonian is block diagonal in this basis. We denote the block of  $S = 0$  by  $\mathcal{M}_s$  and the  $S = 1$  block by  $\mathcal{M}_t$ , referring to singlet and triplet, respectively.

The singlet sector includes the states,

$$\begin{aligned} |\Psi_1^s\rangle &= \frac{1}{\sqrt{2}} \left( |-1, \uparrow\rangle_i \otimes |1, \downarrow\rangle_j - |-1, \downarrow\rangle_i \otimes |1, \uparrow\rangle_j \right) \\ |\Psi_2^s\rangle &= \frac{1}{\sqrt{2}} \left( |1, \uparrow\rangle_i \otimes |-1, \downarrow\rangle_j - |1, \downarrow\rangle_i \otimes |-1, \uparrow\rangle_j \right) \\ |\Psi_3^s\rangle &= \frac{1}{\sqrt{2}} \left( |-1, \uparrow\rangle_i \otimes |-1, \downarrow\rangle_j - |-1, \downarrow\rangle_i \otimes |-1, \uparrow\rangle_j \right) \\ |\Psi_4^s\rangle &= \frac{1}{\sqrt{2}} \left( |1, \uparrow\rangle_i \otimes |1, \downarrow\rangle_j - |1, \downarrow\rangle_i \otimes |1, \uparrow\rangle_j \right), \end{aligned} \tag{S3.1}$$

where  $\pm 1$  denotes the orbital degrees of freedom and the arrows denote the spin. Similarly, we have for the triplet sector with  $S^z = 1$  the states,

$$\begin{aligned} |\Psi_1^t\rangle &= |-1, \uparrow\rangle_i \otimes |1, \uparrow\rangle_j \\ |\Psi_2^t\rangle &= |1, \uparrow\rangle_i \otimes |-1, \uparrow\rangle_j \\ |\Psi_3^t\rangle &= |-1, \uparrow\rangle_i \otimes |-1, \uparrow\rangle_j \\ |\Psi_4^t\rangle &= |1, \uparrow\rangle_i \otimes |1, \uparrow\rangle_j \end{aligned} \tag{S3.2}$$

We start with the intersite Coulomb interaction denoted by  $V_C$  which contributes to first order in perturbation theory. We calculate the matrix elements of the intersite Coulomb interaction (using the expressions derived in the previous sections) between states in the ground state manifold  $n, m$ ,  $\mathcal{M}_{mn}^{(1)} = \langle \Psi_m | V_C | \Psi_n \rangle$ .

Next, we consider the effect of the moiré potential, which hops an electron through to a neighboring site and back. This is a second-order process so we need second order degenerate perturbation theory to get  $\mathcal{M}_{mn}^{(2)}$ ,

$$\mathcal{M}_{mn}^{(2)} = \sum_p \frac{\langle m | H_T | p \rangle \langle p | H_T | n \rangle}{E_0 - E_p} \tag{S3.3}$$

where  $|p\rangle$  are virtual states whereby each site holds 2 and 4 electrons.

Phase	$(a_M, \varepsilon_r)$	$J_H$	$J_{zz}^s$	$J_{zz}^o$	$J_+$	$J_{+-}^s$	$J_{++}^s$	$J_{+-}^o$	$J_{++}^o$
FM	(9.0, 5.0)	-2.127	-7.372	-2.60	$-1.549 - 3.675i$	$2.224 + 3.063i$	0.672249	$0.216 + 0.332i$	0.816
Stripe	(7.0, 5.0)	-15.719	-4.417	-0.573	$4.828 - 20.718i$	$3.369 + 16.225i$	-6.00	$0.250 + 0.924i$	0.100
Zigzag	(6.0, 8.0)	0.341	-17.706	-2.838	$-3.688 - 25.438i$	$-2.497 + 20.935i$	8.808	$-0.079 + 0.538i$	2.672
Nematic	(10.0, 9.0)	17.847	-6.679	-1.777	$-11.626 + 11.190i$	$1.233 - 8.318i$	9.719	$0.622 - 1.583i$	2.850
VBS	(6.0, 10.0)	7.270	-29.322	-5.701	$-7.100 - 25.456i$	$-3.312 + 19.191i$	15.086	$-0.194 + 0.262i$	4.359
HSL	(8.0, 7.0)	2.865	-16.153	-4.170	$-4.532 - 9.459i$	$2.572 + 7.520i$	4.497	$0.460 + 0.790i$	2.086

TABLE I. Numerical values of the Couplings (in meV) representative for the different phases found in DMRG and the corresponding values of  $a_M$  (in nm) and  $\varepsilon$

We can parametrize the two matrices  $\mathcal{M}_\alpha$  by,

$$\mathcal{M}_\alpha = \begin{pmatrix} \mathcal{M}_{\alpha}^{11} & \mathcal{M}_{\alpha}^{12} & \mathcal{M}_{\alpha}^{13} & \mathcal{M}_{\alpha}^{13*} \\ \mathcal{M}_{\alpha}^{12*} & \mathcal{M}_{\alpha}^{11} & \mathcal{M}_{\alpha}^{13*} & \mathcal{M}_{\alpha}^{13} \\ \mathcal{M}_{\alpha}^{13*} & \mathcal{M}_{\alpha}^{13} & \mathcal{M}_{\alpha}^{33} & \mathcal{M}_{\alpha}^{34} \\ \mathcal{M}_{\alpha}^{13} & \mathcal{M}_{\alpha}^{13*} & \mathcal{M}_{\alpha}^{34} & \mathcal{M}_{\alpha}^{33} \end{pmatrix}, \quad (\text{S3.4})$$

where  $\alpha$  denotes  $s, t$ . A general 16 by 16 matrix is spanned by 256 tensor product of Pauli matrices and the identity matrix. We set  $\mathcal{M}$  equal to a linear combination of these matrices,

$$\mathcal{M} = \sum_{\alpha\beta\gamma\delta} J_{\alpha\beta\gamma\delta} S_i^\alpha \otimes \eta_i^\beta \otimes S_j^\gamma \otimes \eta_j^\delta. \quad (\text{S3.5})$$

The solution to the set of linear equations obtained from Equation (S3.5) indeed gives the only terms allowed by symmetry, and in terms of  $\mathcal{M}_{ij}$ , they are:

$$\begin{aligned} J_H &= \frac{1}{2} (\mathcal{M}_t^{11} + \mathcal{M}_t^{33} - \mathcal{M}_s^{11} - \mathcal{M}_s^{33}) \\ J_{zz}^s &= \frac{1}{2} (\mathcal{M}_t^{33} - \mathcal{M}_t^{11} + \mathcal{M}_s^{11} - \mathcal{M}_s^{33}) \\ J_{zz}^o &= \frac{1}{8} (\mathcal{M}_s^{33} - \mathcal{M}_s^{11} + 3\mathcal{M}_t^{33} - 3\mathcal{M}_t^{11}) \\ J_+ &= \frac{1}{2} (\mathcal{M}_t^{13*} - \mathcal{M}_s^{13*}) \\ J_{+-}^s &= \frac{1}{4} (\mathcal{M}_t^{12*} - \mathcal{M}_s^{12*}) \\ J_{++}^s &= \frac{1}{4} (\mathcal{M}_t^{34} - \mathcal{M}_s^{34}) \\ J_{+-}^o &= \frac{1}{16} (3\mathcal{M}_t^{12*} + \mathcal{M}_s^{12*}) \\ J_{++}^o &= \frac{1}{16} (3\mathcal{M}_t^{34} + \mathcal{M}_s^{34}) \end{aligned} \quad (\text{S3.6})$$

We show how the couplings vary as a function of  $a_M$  and  $\varepsilon_r$  in Fig. S5. The numerical values of the couplings for representative points in the phase diagram are shown in TABLE I.

## IV. CLASSICAL GROUND STATE OPTIMIZATION

### A. Setup and method

In order to build an understanding of the model in Eq. 3, we begin by looking the minimal energy “ground state” configurations of its classical limit, where the components of  $\mathbf{S}$  and  $\boldsymbol{\eta}$  are  $c$ -numbers. We assume that the classical ground states retain some subgroup (the translation-breaking pattern) of the full plane group  $p31m$ , and so are characterized by  $\mathbf{S}$  and  $\boldsymbol{\eta}$  on each of  $n$  sublattices. For a particular symmetry-breaking pattern, the classical Hamiltonian is a function  $\mathcal{H}(\{\boldsymbol{\eta}_i\}, \{\mathbf{S}_i\})$  from the product manifold  $(S^2)^{\times 2n}$  of  $2n$  spheres, one for pseudospin  $\boldsymbol{\eta}$  and one for spin  $\mathbf{S}$  on each sublattice, to the reals (the energy of the configuration). We then minimize this Hamiltonian

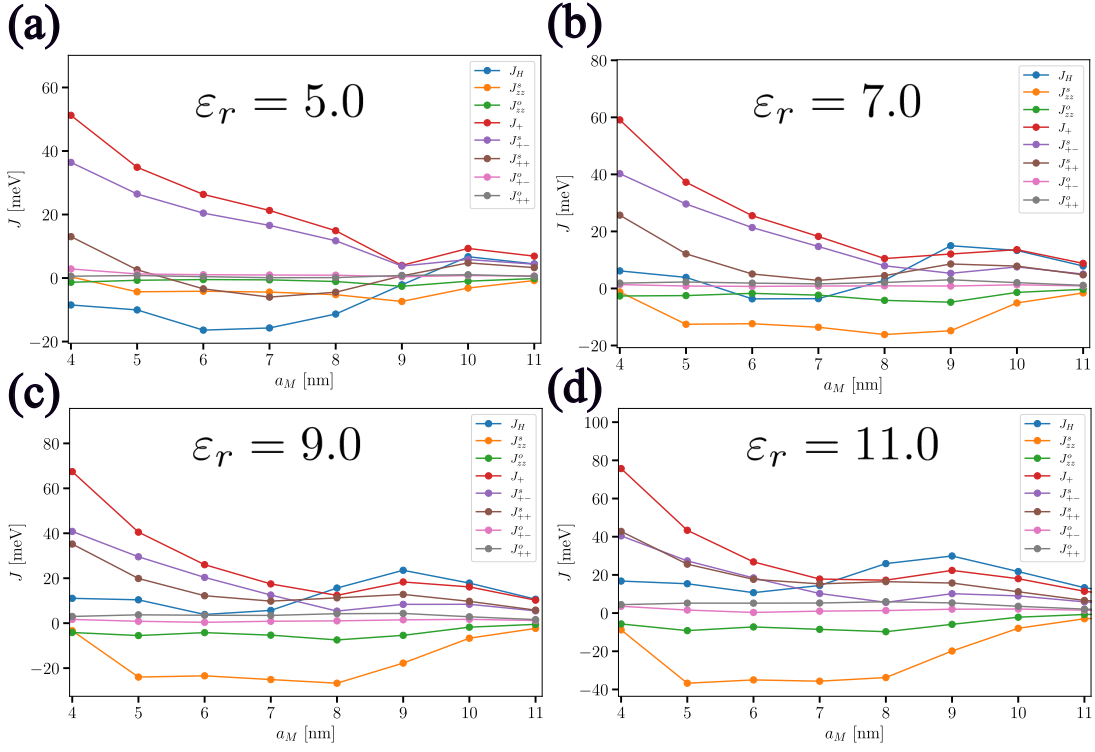


FIG. S5. (a)-(d) The dependence of the couplings  $J$  as the moiré scale  $a_M$  is varied at four different values of  $\epsilon_r$ .

function using manifold conjugate gradient descent [S61–S63]. As a nonconvex optimization problem, this has no robust guarantees of convergence, but we run the optimization many times from random starting configurations in order to be confident that we’ve found the global minimum energy. This becomes more difficult for translation-breaking patterns with much more than twelve sites, but most of our optimal states are well below that size. We can finally compare the lowest energies attained by each symmetry-breaking pattern to classify the phases by their symmetry, resulting in the classical phase diagram in Fig. 3(a). In addition, we are able to compare the energies obtained from DMRG and classical optimization, as shown in Fig. S7(a).

### B. Fully-classical optimization

We probe translation-breaking patterns with up to twelve-site unit cells. The crosshatched region of the classical phase diagram of Fig. 3 is the region where six-, nine-, or twelve-site translation-breaking patterns have the lowest energy. This suggests that either the true ground-state configuration has an even bigger unit cell or that its order is incommensurate with the lattice spacing. Below we comment on the form of several of the classical phases in particular and discuss qualitatively how they arise from the couplings in Table I.

The Stripe and FM phases are the same as those that appear in the quantum model, and their configurations are shown in Fig. 3(a). There are two more phases that are only present in the classical configuration: an antiferromagnetic/ferroelectric (AFM/FE) and an antiferromagnetic/antiferroelectric (AFM/AFE). These configurations are shown in Fig. S6.

*Ferromagnet.*—The FM phase breaks time-reversal and exhibits a homogenous spin alignment, preserving both the translation and point group symmetries. In our model, the orbital degrees of freedom also order, with  $\eta^z \neq 0$  in both the quantum and classical settings. We emphasize that such an orbital ordering does not signal a ferroelectric phase; unlike the in-plane component  $\eta_{\parallel}$  with is  $\mathcal{T}$ -symmetric,  $\eta^z$  maps to  $-\eta^z$  under time-reversal. The dominant couplings at the FM points are  $J_H$ ,  $J_{zz}^s$ , and  $J_{zz}^o$ , all of which are real and negative, preferring mutually reinforcing Heisenberg and Ising ferromagnets in the  $\mathbf{S}$  and  $\eta^z$  sectors, respectively.

*Stripe.*—The origin of the stripe phase can be understood in terms of the dominant  $H_+$  term, which couples linearly the in-plane orbital degrees of freedom with the spin-spin correlations. In this section, we argue that the Stripe configuration is a likely candidate to be the ground state of  $H_+$  via a self-consistent optimization of the  $\mathbf{S}$  and

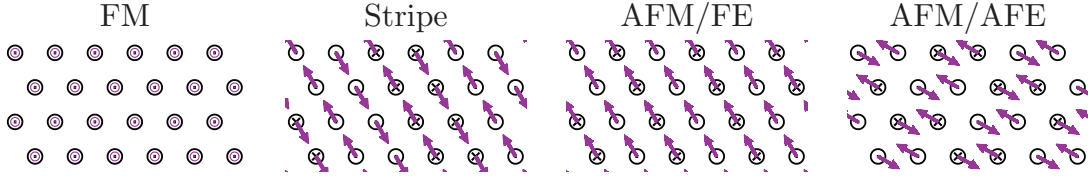


FIG. S6. The classical optimization finds four phases, two of which are also present in the quantum phase diagram. FM and Stripe are just the same as in Fig. 3. The new phases are antiferromagnetic/ferroelectric (AFM/FE) with a two-site unit cell and antiferromagnetic/antiferroelectric (AFM/AFE) with a four-site unit cell and rectangular translation symmetry. Both of these phases include some degree of in-plane canting in some parts of the diagram, meaning that they can have noncollinear  $\boldsymbol{\eta}$  (not shown in these representative configurations). Both of them are overwhelmed in the quantum phase diagram by phases with entanglement, inaccessible to purely classical optimization.

$\boldsymbol{\eta}$  degrees of freedom independently.

It is useful to write the Hamiltonian in terms of Cartesian spin coordinates  $\boldsymbol{\eta}$  instead of ladder operators  $\eta^\pm$  of Eq. 3. The couplings in the stripe region of the phase diagram is dominated by  $J_+$ , with  $J_{+-}^s$  and  $J_H$  also important. These each multiply a Heisenberg term  $\mathbf{S}_i \cdot \mathbf{S}_j$ , and the  $\boldsymbol{\eta}$  pieces of the  $J_+$  and  $J_{+-}^s$  contributions in Cartesian notation are

$$\begin{aligned} H_+ &= 2 \operatorname{Re}(J_+) [\mathbf{a}_{ij} \cdot (\boldsymbol{\eta}_i + \boldsymbol{\eta}_j)] + 2 \operatorname{Im}(J_+) [\mathbf{a}_{ij} \times (\boldsymbol{\eta}_i - \boldsymbol{\eta}_j)] \cdot \hat{z} \\ H_{+-}^s &= 2 \operatorname{Re}(J_{+-}^s) [\boldsymbol{\eta}_i \cdot \boldsymbol{\eta}_j - \eta_i^z \eta_j^z] + 2 \operatorname{Im}(J_{+-}^s) [\boldsymbol{\eta}_i \times \boldsymbol{\eta}_j] \cdot \hat{z} \end{aligned} \quad (\text{S4.1})$$

where  $\mathbf{a}_{ij}$  is the bond vector from site  $i$  to site  $j$ . The imaginary parts of  $J_+$  and  $J_{+-}^s$  are much larger than their real parts in the Stripe region, so we will focus on these.

Firstly, we note that in order to take energetic advantage of the coupling with the largest magnitude,  $J_+$ , we can have neither uniform, ferroelectric  $\boldsymbol{\eta}$  nor a uniform, ferromagnetic  $\mathbf{S}$ . In the ferroelectric, the term  $(\boldsymbol{\eta}_i - \boldsymbol{\eta}_j)$  would always be zero, while a ferromagnetic  $\mathbf{S}$  configuration has uniform  $\mathbf{S}_i \cdot \mathbf{S}_j$ , meaning that the sum over  $H_+$  is

$$\sum_{\langle ij \rangle} H_+ \mathbf{S}_i \cdot \mathbf{S}_j \propto \sum_{\langle ij \rangle} (\mathbf{a}_{ij} \times \boldsymbol{\eta}_i - \mathbf{a}_{ij} \times \boldsymbol{\eta}_j) \cdot \hat{z} = 0, \quad (\text{S4.2})$$

as each site appears an equal number of times as  $i$  and as  $j$ .

Next we ask if there exists a configuration of spins and  $\boldsymbol{\eta}$  which minimizes this term self-consistently.  $H_+$  is linear in  $\boldsymbol{\eta}$  and it couples to a Heisenberg term  $\mathbf{S}_i \cdot \mathbf{S}_j$  that's quadratic in  $\mathbf{S}$ . Under a fixed  $\boldsymbol{\eta}$  configuration, this is a Heisenberg model for  $\mathbf{S}$  with a bond-dependent coupling. Under a fixed  $\mathbf{S}$  configuration,  $\boldsymbol{\eta}$  only experiences an “external field” generated by nonuniform  $\mathbf{S}$  correlations. If  $\mathbf{S}$  manages to be a ground state of the Heisenberg model generated by  $\boldsymbol{\eta}$ , and simultaneously  $\boldsymbol{\eta}$  is parallel to the site-dependent field generated by  $\mathbf{S}$ , the state is self-consistent and stable under  $H_+$ .

In the observed ground state (Fig. S6), we observe unit-period transverse ferroelectricity in  $\boldsymbol{\eta}$  along with doubled-period antiferromagnetism in  $\mathbf{S}$  with both ferromagnetic and antiferromagnetic correlations. The Heisenberg coupling generated by  $\boldsymbol{\eta}$  along the stripe is zero. Perpendicular to the stripes, the Heisenberg coupling is nonzero because  $\boldsymbol{\eta}_i - \boldsymbol{\eta}_j$  isn't parallel to  $\mathbf{a}_{ij}$ , and it alternates sign along with  $\boldsymbol{\eta}$ . This gives rise to the double-wide stripes in  $\mathbf{S}$ , with alternating spin-spin correlations—this is evidently the unique classical ground state of the effective Heisenberg model generated by the configuration up to  $\text{SU}(2)_s$ .

Any particular site  $i$  has neighbors in the  $\pm \mathbf{a}_J$  directions for  $J = 1, 2, 3$ , which we'll denote here for brevity as  $\mathbf{S}_{i \pm J}$ .  $H_+$  acts linearly on its orbital pseudospin  $\boldsymbol{\eta}_i$ , so we have

$$2 \operatorname{Im} J_+ \sum_{\langle ij \rangle} \hat{z} \cdot (\mathbf{a}_{ij} \times (\boldsymbol{\eta}_i - \boldsymbol{\eta}_j)) (\mathbf{S}_i \cdot \mathbf{S}_j) = 2 \operatorname{Im} J_+ \sum_i \sum_{J=1}^3 (\mathbf{S}_i \cdot (\mathbf{S}_{i+J} - \mathbf{S}_{i-J})) (\hat{z} \times \mathbf{a}_J) \cdot \boldsymbol{\eta}_i. \quad (\text{S4.3})$$

In our ground state configuration, the external field on  $\boldsymbol{\eta}_i$  only receives contributions for bonds  $J$  that are not in the stripe direction. Each of these is in the direction  $\hat{z} \times \mathbf{a}_J$ , perpendicular to its bond, but the signs of the spin-spin correlations are such that in total, the components of the field perpendicular to the stripe cancel, and the  $\boldsymbol{\eta}$  order is stabilized self-consistently.

We must also make sure that this order isn't strongly opposed or altered by  $J_H$  or  $J_{+-}^s$ , the other two pertinent couplings. The negative  $J_H$  would prefer an  $\mathbf{S}$ -ferromagnet, but this is incompatible with the energetic gains to be



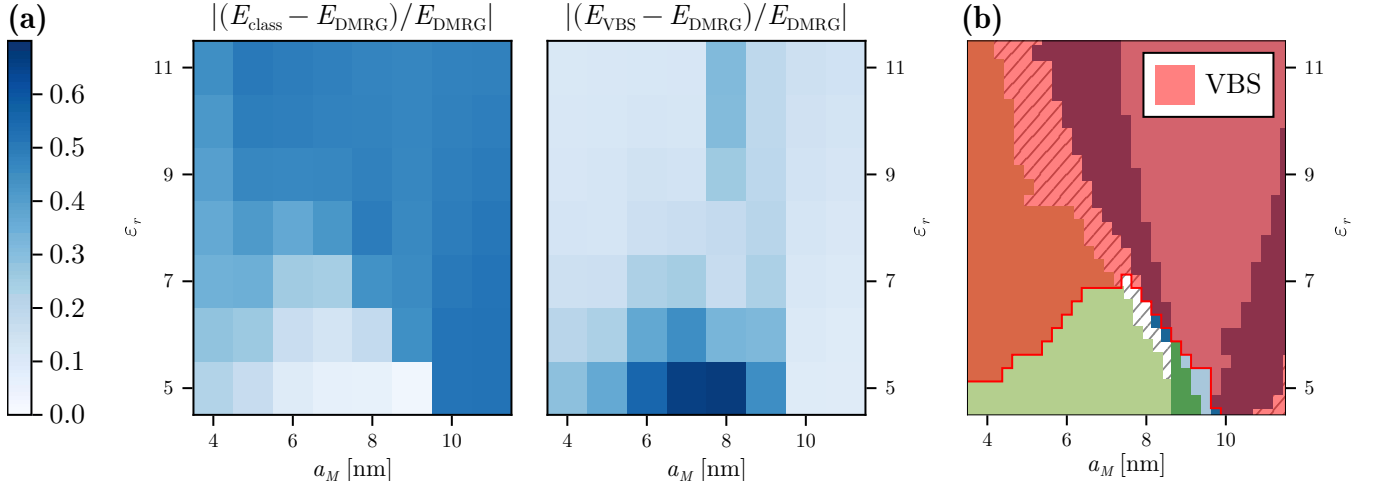


FIG. S7. (a) The classical ground states only give good approximations to DMRG energetics in the Stripe and FM phases. The VBS ansatz is able to get an energy similar to that from DMRG in the FiE-VBS, Nematic, and Zigzag regions. (b) The VBS semiclassical ansatz dominates the semiclassical phase diagram in all regions except near the Stripe and FM phases.

made from  $J_+$  as discussed above, so it must be satisfied that spin-spin correlations are ferromagnetic along two-thirds of the bonds. The imaginary part of  $J_{+-}^s$  multiplies the term  $(\boldsymbol{\eta}_i \times \boldsymbol{\eta}_j) \cdot \hat{z}$ , which is zero uniformly for the Stripe, as the  $\boldsymbol{\eta}$  pattern is collinear.

*AFM/FE and AFM/AFE.* We will not discuss these phases in detail, as they are less physically relevant. In particular, as discussed in the main text, we found that these phases are destabilized by quantum fluctuations. In the AFM region of the classical diagram, the  $J_H$  term is dominant and antiferromagnetic, which leads to the overall frustrated antiferromagnetism in  $\mathbf{S}$ . The role of the many other terms in setting the boundaries is less clear or important.

### C. Semiclassical optimization with a VBS ansatz.

Of the quantum phases, only Stripe and FM are directly accessible as classical configurations. The Nematic and Zigzag phases are Luttinger-like, so they don't support a mean-field description. However, the FiE-VBS phase can still be examined semiclassically by fixing a pattern of  $\mathbf{S}$ - $\mathbf{S}$  singlets and then minimizing the energy over the  $\boldsymbol{\eta}$  pseudospins: from the perspective of classical  $\boldsymbol{\eta}$ , it's no object that the singlet correlations  $\langle \mathbf{S}_i \cdot \mathbf{S}_j \rangle = -3/4$  are able to exceed classical bounds, and the optimization can proceed in the same way. When we do this, we see that the VBS configuration has a lower energy than any other classical configuration in most of the phase diagram—all of it except the Stripe and FM regions, as shown in Fig. S7. The  $\langle \boldsymbol{\eta} \rangle$  pattern is the same as that that we see in iDMRG. Note that the Helical SL phase emerges in the region of the semi-classical phase diagram that borders Stripe, FM, FiE-VBS, and the unconverged sliver, in line with our expectation that such a state be enabled by great frustration.

We also use this semiclassical approach to test “brick wall” VBS patterns, where the singlets are all aligned in the same direction. Neither of the two distinct brick-wall VBS ansätze have a favorable energy anywhere in the diagram. This supports the idea that the Nematic and Zigzag states that we see with DMRG are truly Luttinger-like, instead of just being a cat state of translation-breaking VBS states along the short axis of the cylinder.

## V. DMRG METHODOLOGY AND RESULTS

To find the quantum phase diagram in Fig. 3, we use the infinite density-matrix renormalization group (iDMRG) as implemented in TenPy [S70], performed on a cylinder of circumference  $L_y = 4, 6$  and with  $U(1)_s$ -symmetric tensors of bond dimension up to  $\chi = 2560$ .

*Cylinder geometry.* We wrap the triangular lattice such that the  $\pm \mathbf{a}_1$  direction runs along the cylinder and the  $\pm \mathbf{a}_3$  direction wraps around it: a translation of  $\pm L_y \mathbf{a}_3$  carries a site back to where it started. We use a matrix product state unit cell of  $L_x L_y$  independent tensors, where  $(L_x, L_y) = (2, 4)$  or  $(1, 6)$ . This cylinder geometry breaks  $C_{3v}$ ,

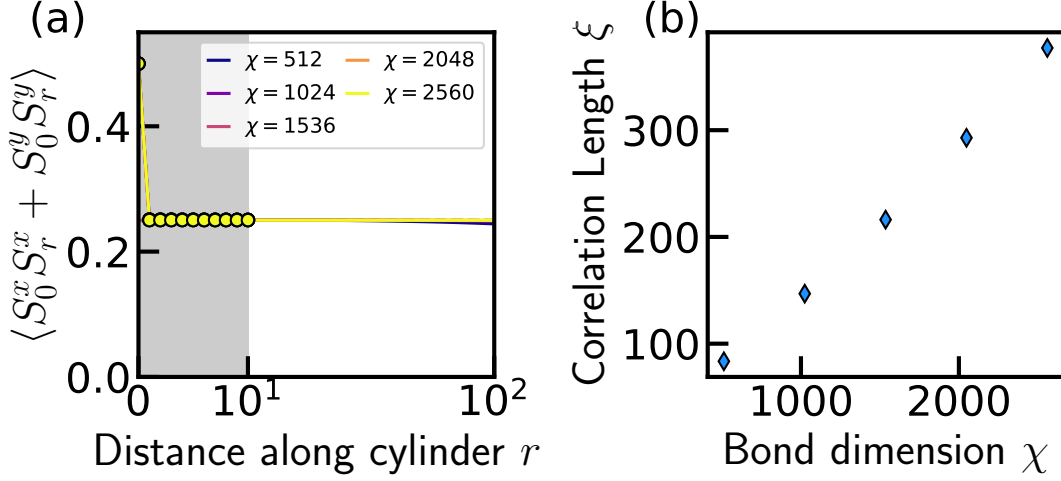


FIG. S8. (a) Two-point spin-spin correlation function for  $(a_M, \epsilon_r) = (9.0, 5.0)$  for a  $L_y = 4$  cylinder. We observe that the system exhibits extremely long-ranged correlations, consistent with the presence of an ordered state. (b) Formally, the iDMRG simulation encodes a one dimensional problem, so true long-range order cannot be supported by the system. Indeed, we observe an increasing correlation length with increasing bond-dimension, capturing expected quasi-long-range order of the two-point correlation function in a one dimensional system with U(1) symmetry.

of course, but it actually preserves the mirror that maps  $\mathbf{a}_3 \mapsto -\mathbf{a}_3$ , which we'll notate as  $M_3$ . We run DMRG on all points for  $L_y = 4$ , but we make additional runs at  $L_y = 6$  for points near phase boundaries and to make sure that our phases aren't being "trapped" by the finite cylinder size, which lets us get a better handle on the physical picture in the thermodynamic limit.

### A. Correlation data and pinning fields

In this section, we present the correlation data that we obtain in each classical phase, addressing issues of convergence as necessary.

*Pinning fields.* The Mermin-Wagner theorem forbids spontaneous breaking of a continuous symmetry in a classical two-dimensional statistical model at finite temperature [S55]. By the quantum-to-classical mapping, it can be shown that the quantum path integral that generates the ground-state properties of our model on a finite-circumference infinite-length cylinder is equivalent to a classical thermal path integral for a two-dimensional system at finite temperature—under a Wick rotation, the finite circumference goes to a Euclidean time/inverse temperature  $\beta$ , and the infinite time dimension becomes an infinite spatial dimension. Therefore, we shouldn't expect to observe states that break SU(2) in DMRG, even if they would actually be symmetry-broken in the thermodynamic limit of a fully two-dimensional quantum system with infinite extent.

This is relevant to our work only in the Stripe and Helical SL phases, both of which break SU(2)<sub>s</sub>. While FM breaks SU(2)<sub>s</sub>, we're able to see this directly by using tensors that fix the overall  $S^z$  sector to be fully-polarized. The difference is that while Stripe and Helical SL break SU(2)<sub>s</sub>, their order parameters do not themselves generate a symmetry of the Hamiltonian, so they do not generate suitable conserved quantities for quantum number-conserving DMRG. One possible solution is to use a pinning field (e.g., as done in Ref. S89 to see AFM order): we add a term to the Hamiltonian which couples directly to the order parameter that we're interested in, which allows us to measure its susceptibility. In a disordered state, we'd expect the susceptibility to be finite and analytic as the field is swept through zero. If the susceptibility diverges near zero applied field, we have a state with long-range order, even if DMRG is not able to resolve that order in a quasi-one-dimensional setting.

#### 1. Ferromagnet (FM)

The FM phase breaks time-reversal  $\mathcal{T}$  and spin-rotation SU(2)<sub>s</sub> while preserving the space group. In the sector with total spin  $S^z = 0$ , the iDMRG wavefunction is unable to express a nonzero local expectation value  $\langle \mathbf{S}_\perp \rangle$  since  $S_\perp$  is an

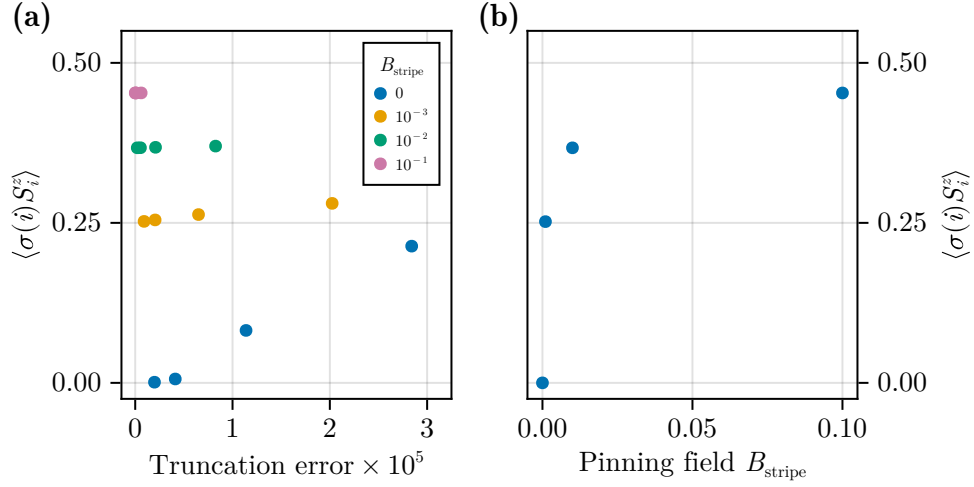


FIG. S9. By adding a pinning field  $B_{\text{stripe}}$ , we can see the diverging susceptibility that indicates spontaneous symmetry breaking, even when the Mermin-Wagner theorem prohibits spontaneous breaking of a continuous symmetry in our quasi-one-dimensional setting. The values in (b) are linear extrapolations to zero truncation error of the measured data in (a).

operator without definite U(1) charge. However, the FM order will be manifest in the presence of long-range spin-spin correlations,  $\langle S_0^x S_r^x + S_0^y S_r^y \rangle$  [Fig. S8(a)]. However, one must be careful—the iDMRG formally defines an effective one dimensional quantum problem that cannot, via the Mermin-Wagner theorem, exhibit long-range order when breaking a continuous symmetry [in this case U(1)]. Indeed, we observe that the correlation length of the system remains finite and grows with increasing bond dimension [Fig. S8(b)]. These are known signatures of continuous symmetry breaking in iDMRG. With respect to the orbital degrees of freedom, we observe almost complete polarization along the orbital pseudospin quantization axis, with  $\langle \eta^z \rangle = 0.97294$ .

## 2. Stripe

The Stripe phase has a four-site unit cell, breaking the point group  $C_{3v}$ , time-reversal  $\mathcal{T}$ , and spin rotation  $\text{SU}(2)_s$ . Our Stripe ordering is along the cylinder in the  $\mathbf{a}_1$  direction. The antiferroelectric order parameter is almost classical at  $\langle \mathbf{a}_1 \cdot \boldsymbol{\eta} \rangle = \langle \eta^x \rangle = \pm 0.983$ . Because the Stripe phase breaks the continuous symmetry  $\text{SU}(2)_s$ , we observe the symmetry breaking by applying a straightforward pinning field of the form

$$H_{\text{stripe}} = B_{\text{stripe}} \sum_i (-1)^{\sigma(i)} S_i^z, \quad \sigma(i) = \begin{cases} 0 & (\vec{r}_i \cdot \vec{a}_1) \bmod 4 = 0 \text{ or } 1 \\ 1 & (\vec{r}_i \cdot \vec{a}_1) \bmod 4 = 2 \text{ or } 3 \end{cases}, \quad (\text{S5.1})$$

where  $\vec{r}_i$  is the position of the  $i$ th lattice point. This favors the Stripe order on  $S$ . We extrapolate on truncation error to estimate the Stripe order parameter at infinite bond dimension. These results are presented in Fig. S9, which demonstrates that the susceptibility  $\chi_{\text{stripe}} = \frac{\partial \langle \sigma(i) S_i^z \rangle}{\partial B_{\text{stripe}}}$  is very large at zero field. This data is computed for  $L_y = 4$ , but we expect the curve to become a step function in the thermodynamic limit as  $L_y$  goes to infinity.

## 3. Ferrielectric Valence Bond Solid (FiE-VBS)

The FiE-VBS state breaks only space group symmetries, maintaining time-reversal  $\mathcal{T}$  and spin-rotation  $\text{SU}(2)_s$ . We measure the spin correlations between bonded sites as  $\langle \mathbf{S}_i \cdot \mathbf{S}_j \rangle = -0.568$ , reduced in magnitude from the  $-3/4$  of an ideal singlet. The state is ferrielectric because it has a net average moment per site of  $\langle \boldsymbol{\eta} \rangle_i = 0.152 \mathbf{a}_1$ . The residual antiferroelectricity after this moment is subtracted off is close to a four-sublattice  $90^\circ$  pattern [Fig. S10].

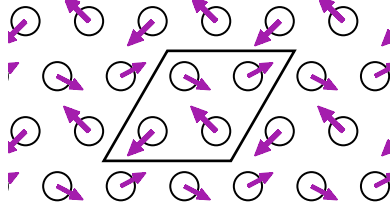


FIG. S10. After subtracting off the net ferroelectric moment, the remaining  $\langle \boldsymbol{\eta}_{\parallel} \rangle$  of the FiE-VBS state approaches a four-sublattice  $90^\circ$  ordering pattern.

#### 4. Helical Spin Liquid (HSL)

The Helical SL phase also breaks  $SU(2)_s$ , but we do not see the susceptibility diverge as cleanly as we do in the Stripe. The HSL pinning field is

$$H_{\text{HSL}} = B_{\text{HSL}} \sum_{\langle ij \rangle} C_{ij}^z = B_{\text{HSL}} \sum_{\langle ij \rangle} (\mathbf{S}_i \times \mathbf{S}_j)^z, \quad (\text{S5.2})$$

which is notably different from  $H_{\text{stripe}}$  in that the terms on different bonds in the external field Hamiltonian don't commute with each other. This means that we don't have a clear picture of a mean-field Hamiltonian with a simple, unentangled ground state, as we do in most cases of spontaneous symmetry breaking. That being said, we can still check the dependence of the order parameter on the field to check for signs of symmetry-breaking.

The results are shown in Fig. S11. At moderate fields, the helical order parameter converges cleanly in truncation error to a finite extrapolant, as is the case for the Stripe. At smaller fields, the approach is more nonlinear, so we can't be as confident about our extrapolation. For the fields down to  $B_{\text{HSL}} = 0.0025$  that we have investigated, though, the order parameter seems to converge, and above all else it is clear that the value of the order parameter is significantly higher for  $L_y = 6$  than  $L_y = 4$ . This supports our claim that the operator  $C_{ij}^z$  orders spontaneously in the full  $L_y \rightarrow \infty$  thermodynamic limit.

The cylinder geometry explicitly breaks the point group symmetry  $C_{3v}$ , but it preserves the  $\mathbf{a}_3 \mapsto -\mathbf{a}_3$  mirror  $M_3$ , as discussed above. Due to this finite-size effect, that our DMRG results display a small in-plane pseudospin expectation value  $\langle \boldsymbol{\eta}_{\parallel} \rangle$  which is approximately proportional to  $\mathbf{a}_3$ . The  $M_3$ -breaking component perpendicular to  $\mathbf{a}_3$  goes to zero with truncation error, and the magnitude of this vector goes to zero as the cylinder circumference goes to infinity and full  $C_{3v}$  is restored. For  $L_y = 6$  at  $\chi = 2560$  in particular, the average  $M_3$ -preserving component  $\langle \boldsymbol{\eta}_{\parallel} \rangle \cdot \mathbf{a}_3$  is  $2.1 \times 10^{-2}$ , and the average  $M_3$ -breaking component  $|\langle \boldsymbol{\eta}_{\parallel} \rangle \times \mathbf{a}_3|$  is  $1.9 \times 10^{-4}$ .



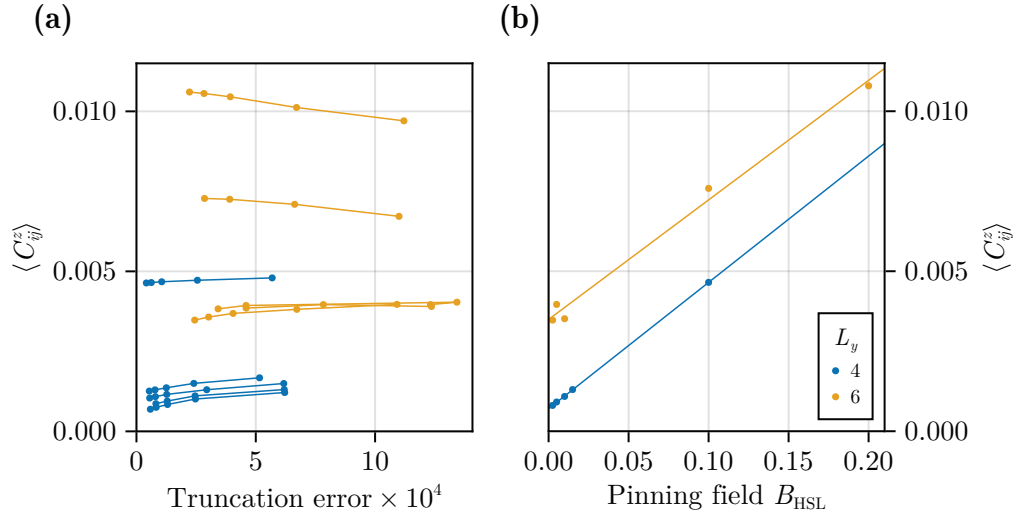


FIG. S11. Similarly to the Stripe case, the HSL order can be stabilized by adding a pinning field  $B_{HSL}$ . In (a), the measured order parameter  $\langle C_{ij}^z \rangle$  is plotted as a function of truncation error for various pinning fields. The approach to zero is not as linear as in the Stripe, so the extrapolated values of  $\langle C_{ij}^z \rangle$  are plotted with uncertainties computed from the dependence of the extrapolated value on the number of points of different bond dimension/truncation error used in the extrapolation.